Research article

Preliminary investigation of nitric oxide release from upconverted nanoparticles excited at 808 nm near-infrared for brain tumors

Lei Li [a,1], Jiang-hua Yang [b,1], Xin-meng Fa [b], Ming-song Liu [a], Qi-lin Wang [a], Tong-fei Zeng [a], Rui-zhe Chen [a], Jun Ou [b,**], Xue-wei Xia [a,*]

[a] Department of Neurosurgery, Affiliated Hospital of Guilin Medical University, 541001, Guilin, China
[b] Materials Science and Engineering College, Guilin University of Technology, 541004, Guilin, China

A R T I C L E   I N F O

A B S T R A C T

Upconverted UCNPs@mSiO$_2$-NH$_2$ nanoparticles were synthesized via thermal decomposition while employing the energy resonance transfer principle and the excellent near-infrared (NIR) light conversion property of up-conversion. The 808 nm NIR-excited photocontrolled nitric oxide (NO) release platform was successfully developed by electrostatically loading photosensitive NO donor Roussin's black salt (RBS) onto UCNPs@mSiO$_2$-NH$_2$, enabling the temporal, spatial, and dosimetric regulation of NO release for biological applications of NO. The release of NO ranged from $0.015 \sim 0.099$ mM under the conditions of 2.0 W NIR excitation power, 20 min of irradiation time, and UCNPs@mSiO$_2$-NH$_2$&RBS concentration of $0.25 \sim 1.25$ mg/mL. Therefore, this NO release platform has an anti-tumor effect. *In vitro* experiments showed that under the NIR light, at concentrations of 0.3 mg/mL and 0.8 mg/mL of UCNPs@mSiO$_2$-NH$_2$&RBS, the activity of glioma (U87) and chordoma (U–CH1) cells, as measured by CCK8 assay, was reduced to 50 %. Cell flow cytometry and Western Blot experiments showed that NO released from UCNPs@mSiO$_2$-NH$_2$&RBS under NIR light induced apoptosis in brain tumor cells. *In vivo* experiments employing glioma and chordoma xenograft mouse models revealed significant inhibition of tumor growth in the NIR and UCNPs@mSiO$_2$-NH$_2$&RBS group, with no observed significant side effects in the mice. Therefore, NO released by UCNPs@mSiO$_2$-NH$_2$&RBS under NIR irradiation can be used as a highly effective and safe strategy for brain tumor therapy.

1. Introduction

Glioma, accounting for about 40 % of intracranial tumors, is a common malignant tumor of the nervous system [1,2]. It is characterized by infiltrative growth, frequent in situ recurrence, high recurrence rate, and poor prognosis despite various interventions such as surgery, radiotherapy, or chemotherapy [3–5]. Chordoma is a relatively rare and destructive intracranial tumor that grows invasively, and the expected failure rate of marginal resection is 18 %–89 %, depending on the location, size, and degree of infiltration of the tumor [6]. In recent years, photodynamic therapy (PDT) has emerged as a highly promising novel anti-glioma therapy [7–10]. However, challenges such as the reduced oxygen supply localized to the tumor during treatment [11] and the limitation of the laser

---

* Corresponding author. Department of Neurosurgery, Affiliated Hospital of Guilin Medical University, 541001, Guilin, China.
** Corresponding author.
E-mail addresses: yjgch1226@163.com (J. Ou), m18404995328_1@163.com (X.-w. Xia).
[1] These authors contributed equally to this work.

tissue penetration depth to 1–5 mm [12], hinder the complete treatment of the tumor. Therefore, improving the limited penetration depth of the laser and finding a new approach have become key aspects in the treatment of brain tumors.

Gas therapy has attracted greater scientific attention in the treatment of various diseases, and the controlled release of gases has been of significant importance in biomedicine [13]. Upconversion nanoparticles (UCNPs) convert long wavelengths of light, characterized by strong tissue penetration, into shorter wavelengths of light capable of inducing the release of gas from photosensitive donors. Therefore, gas therapy combined with UCNPs can achieve NIR excitation and controlled release, thus offering potential applications for cancer therapy [14], bacterial therapy [15], anti-inflammation [16], and neuromodulation [17]. Gases such as nitric oxide (NO) [13], hydrogen sulfide (H_2S) [18], sulfur dioxide (SO_2) [19], oxygen (O_2) [20], hydrogen (H_2) [21], and carbon monoxide (CO) [22] play important roles in physiological and pathological processes. Based on the unique physical and chemical properties of UCNPs, the developed gas nanoplatforms not only facilitate the delivery of therapeutic gases tailored for personalized treatment but also demonstrate effective accumulation at the diseased tissues. This is achieved through enhanced permeability and retention mechanisms or by incorporating targeted surface modifications [13]. The use of NIR light as an external stimulus in gas therapy strategies has attracted great interest from researchers, offering precise control over the timing and spatial release of gases, thus achieving accurate and predictable gas release.

NO, a physiological signaling molecule, plays an important role in regulating physiological and pathological processes [23]. NO is closely related to cancer biology, and its effect on tumor cell growth is mainly dependent on its concentration [24]. At low concentrations (<1 μM), NO serves as a growth factor, stimulating angiogenesis and facilitating nutrient transport to cells, thereby promoting their rapid growth. However, high concentrations of NO (1 μM to 1 mM) produce reactive nitrogen species, which react with reactive oxygen species and lead to oxidative and nitrosyl reactions. These reactions result in DNA base deamination and enzyme nitrosylation, which leads to the impairment of cellular function and, finally, promotes the apoptosis of tumor cells [25].

To address the limitations of other light sources in terms of tissue penetration depth, this study aims to employ NIR, chosen for its deeper tissue penetration ability and reduced damage to tissues, as an ideal stimulation light source for UCNPs. The developed UCNPs system released NO under NIR irradiation, effectively promoting tumor cell apoptosis through the apoptosis pathway and inhibiting the migration and invasion ability of brain tumor cells.

2. Material and methods

2.1. Preparation of sample stock solutions

Firstly, the mass of the specific lanthanide chloride ions was calculated based on the molar percentage content of the doped lanthanide ions, and then the corresponding mass of doped lanthanide chloride ions was weighed into a 10 mL sample bottle using an electronic balance, and at the same time, deionised water was measured into the sample bottle using a pipette gun, and the solid particles of the chlorinated rare earths were sufficiently ultrasonicated to dissolve the solid particles of the chlorinated rare earths into a homogeneous mixture of the solution, which is the initial aqueous solution of the C UCNPs and the CS UCNPs.

2.1.1. NaGdF4:Er0.02/Yb0.2/Ca0.3 upconversion nanoparticle preparation

Pipette 1 mL of an aqueous solution containing 1 mmol of $LuCl_3 \bullet 6H_2O$ ($GdCl_3 \bullet 6H_2O$:$YbCl_3 \bullet 6H_2O$:$ErCl_3 \bullet 6H_2O$ = 0.48:0.2:0.02) into a 50 mL in a 50 mL three-necked flask, add the glass magnetic rotor, the solution was heated and evaporated to a white powder, then the argon device was connected to the three-necked flask, and argon was kept continuously passed into the three-necked flask, and then 3.75 mL of oleic acid (OA) was added, and heated and stirred to the temperature of the solution of 120 °C, and kept for 30 min to remove the excess water in the oleic acid, so as to make the reaction solution reach the anhydrous and anaerobic environment. Then add calcium oleate and 7.5 mL of 1-octadecene, and the reaction solution was heated to 150 °C, this step of the reaction needs to be maintained for 1 h, to be the end of the reaction solution can be observed as a light yellow liquid and stop heating, cooling to room temperature. 4 mL of methanol solution containing sodium hydroxide (NaOH 2.5 mmol) and ammonium fluoride (NH_4F 4 mmol) was added dropwise with vigorous stirring and increased flow rate of argon, and the temperature of the solution was raised to 60 °C for 30 min to remove the methanol solution, and at the same time the temperature was raised to 100 °C and the reaction was stirred for 30 min to completely remove the methanol solution.

Next, a condensing device was added to the three-necked flask, and under the protection of argon, the temperature of the reaction solution needed to be rapidly increased to 300 °C within 20 min, and the reaction was carried out for 1.5 h to provide high-temperature conditions for the formation of nuclei, and at the end of the reaction, the solution was cooled down to room temperature, and the nanoparticles were precipitated and centrifuged by adding anhydrous ethanol according to the ratio of anhydrous ethanol to the reaction solution = 1:1, and then washed with anhydrous ethanol and cyclohexane. Centrifugation was performed several times and the nanocrystals were dispersed into 4 mL of cyclohexane and set aside.

2.1.2. Preparation of NaGdF4: Er0.02/Yb0.2/Ca0.3@NaYF4 Yb0.05/Nd0.4/Ca0.2 upconversion nanoparticles

A pipette gun was used to remove 1 mL of the initial solution of nucleoshells containing 0.4 mmol of aqueous $LuCl_3$ ($YCl_3 \bullet 6H_2O$: $YbCl_3 \bullet 6H_2O$:$NdCl_3 \bullet 6H_2O$ = 0.35:0.05:0.4) in a 50 mL three-necked flask, and the solution was evaporated to a white powder by heating and stirring. The solution was evaporated to a white powder by stirring, firstly, argon was introduced as a protective gas, then 7.5 mL of oleic acid (OA) was added, and the temperature of the solution was increased to 120 °C by a heating device, and kept for 30 min, so as to remove the water in the oleic acid. Then 15 mL of calcium oleate and 1-octadecene were added to the reaction solution, and the temperature of the solution was raised to 150 °C at the same time, and the reaction was carried out for 1 h. When the reaction

was completed, the heating was stopped and the reaction solution was cooled down to room temperature. The nuclear nanoparticles previously prepared and dissolved in cyclohexane were dispersed ultrasonically and added drop by drop into the reaction solution, while 4 mL of a mixture of sodium hydroxide (NaOH 1 mmol) and ammonium fluoride (NH₄F 1.6 mmol) in methanol prepared in advance was added drop by drop into the reaction solution, and the gas flow rate of argon was increased and the temperature of solution was heated up to 60 °C for 30 min, which was used to remove the cyclohexane and methanol solution, followed by providing the temperature to 100 °C for 1 h, and the reaction solution was depleted of methanol and cyclohexane. The operation was to remove cyclohexane and methanol solution, and then the temperature was provided to 100 °C for 1 h to remove methanol and cyclohexane from the reaction solution. Under sufficient stirring, condensation reflux and argon protection, the temperature of the reaction solution was rapidly increased to 300 °C within 20 min and maintained at this temperature for 1.5 h to fully react the mixed solution. Upon completion of the reaction, the reaction was cooled to room temperature. Anhydrous ethanol was added according to the volume ratio of anhydrous ethanol to reaction solution listed as 1:1 to make the nanocrystals fully precipitated, after centrifugation, the nanocrystals were washed and centrifuged several times using anhydrous ethanol and cyclohexane, and then the white powder was put into a vacuum drying box for spare use.

2.1.3. Preparation of UCNPs@mSiO₂ nanoparticle

Using an electronic balance, 20 mg of UCNPs and 0.1 g of surfactants (cationic surfactants, anionic surfactants, nonionic surfactants, and amphoteric surfactants) were weighed with a 50 mL flask, and 20 mL of deionised water was added and placed on a stirrer and stirred thoroughly, and when the solution did not appear to be foamy, 3 mL of anhydrous ethanol, 150 μL of alkaline solutions (NaOH, NH4OH, TEA) and 20 mL of deionised water, the mixed solution was placed in a water bath with a heating temperature of 70 °C, and the total amount of 50 μL of tetraethyl orthosilicate (TEOS) was added drop by drop for 5 μL/10 min using a pipette gun with vigorous stirring, the heating was stopped at the end of the drop and cooled down to room temperature, and the product was washed and centrifuged in anhydrous ethanol, and put into a vacuum drying oven for drying. Weighed 20 mg of the above product in a single-necked flask, and add 50 mL of anhydrous ethanol containing ammonium nitrate (NH₄NO₃ 0.3 g) in the flask, 60 °C water bath heating mounted on the condensation reflux device, need to be reacted for 2 h, after the end of the time, the temperature of the solution was lowered to room temperature, centrifuged directly, and then centrifuged and washed with anhydrous ethanol for several times, and then put into a vacuum drying oven for drying to obtain the UCNPs@mSiO₂ nanoparticles.

2.1.4. Preparation of UCNPs@mSiO₂-NH₂ nanoparticles

Weigh 20 mg of UCNPs@mSiO₂ nanoparticles powder in a 50 mL flask, add 10 mL of deionised water to fully ultrasonic mixing, followed by the addition of 200 μL of acetic acid solution, and under the condition of rapid stirring, a pipette gun was used to add 80 μL of APTES dropwise, 10 μL/min dropwise, and then the reaction solution was stirred for 12 h. The reaction solution was then centrifuged and collected and washed with deionised water several times, and then put into a vacuum drying box for spare use.

2.1.5. Preparation of RBS

Weigh 1.8 g of sodium nitrite ultrasonically dissolved in 8 mL of deionised water to form a transparent solution, then the solution was poured into a 50 mL two-necked flask, and then 3 mL of aqueous solution of ammonium sulfate with a mass fraction of 22 % and 6 mL of deionised water were added, stirred thoroughly and condensed back to reflux, and the reaction solution was heated in an oil bath to 98 °C, and the reaction was for 1.5 h. After the end of heating, access to argon, adjust the gas flow rate, and then add 32 mL of configured aqueous ferrous sulfate solution (FeSO₄ 4 g) and 4 mL mass fraction of 20 % ammonium hydroxide solution drop by drop, adjust the temperature of the oil bath for 90 °C, the reaction is stopped after 30 min of heating, and then immediately filtered to get the black-brown solution, and then the solution was placed in the condition of 4 °C for 24 h, and then it was clearly observed that there were black-brown solid particles precipitated, and then the solution was filtered in vacuum to get the products, and then the vacuum drying could be obtained after the Hessian salt RBS.

2.1.6. Preparation of NO-releasing platforms for UCNPs@mSiO₂-NH₂&RBS

The main operation of combining RBS with UCNPs@mSiO₂-NH₂ by electrostatic action was as follows: 10 mg of UCNPs@mSiO₂-NH₂ was weighed in a brown round-bottomed flask, 15 mL of deionised water was added to ultrasonicate and mix thoroughly, and 0.7 mg of RBS was weighed in a brown round-bottomed flask, which was then placed in the dark and stirred for 24 h. After that, the product was collected by centrifugation and washed with deionised water, and finally put into a dark vacuum drying box for drying. At the end of the time, the product was collected by centrifugation and washed by adding deionised water, and finally the product was put into a dark vacuum drying oven to dry, followed by placing it into a refrigerator for spare use.

2.1.7. Chemicals and reagents

UCNPs@mSiO₂-NH₂, UCNPs@mSiO₂-NH₂&RBS and RBS were respectively dissolved in phosphate buffer (PBS) and uniformly suspended in an ultrasonic cleaner (YM-020S) for subsequent experiments. The final concentration of U87 cells was 0.3 mg/mL, and that of U–CH1 cells was 0.8 mg/mL. The CCK-8 kit was obtained from MedChemExpress. Primary antibodies (Caspase 3, Ki-67) and β-actin (43KD) were purchased from Proteintech, China. Calcein-AM/PI staining solution and gentian violet staining solution were purchased from Solarbio (Beijing, China). Hoechst 33342 was purchased from Shanghai Biyuntian (yeyotime). The Annexin V-FITC/PI Apoptosis Detection Kit was purchased from BD Biosciencesgon, USA.BALB/c mice were purchased from Hunan Slaughter Kingda.

2.2. Cell culture

The human U87 cell line was kindly donated by Southern Medical University and the U–CH1 cell line was kindly donated by Johns Hopkins University. All cell lines were cultured in DMEM containing 10 % fetal bovine serum (Gibco, USA) at 37 °C and 5 % CO_2 in an incubator (IC0150).

2.2.1. The viability of U87 and U–CH1 cells was detected by CCK-8 assay

U87 and U–CH1 cells in logarithmic growth phase were inoculated in 96-well plates for 24 h with approximately 3000 cells per well. The NO release process was as follows: U87 and U–CH1 cells were incubated with different concentrations of UCNPs@mSiO$_2$-NH$_2$, UCNPs@mSiO$_2$-NH$_2$&RBS, and RBS for 24h, respectively. The cells were washed twice with PBS and the medium was replaced with additional DMEM containing 10 % serum, and then the samples were irradiated with a laser with an energy density of 150 J/cm^2 for 10 min in the dark, at the end of the light, the samples were put back into the incubator to continue incubation, and the next cell activity detection experiment was carried out 24 h later. All cell samples were washed twice with PBS, and 100 μL of 10 % CCK-8 reagent (containing 10 μL of CCK-8 reagent + 90 μL of complete culture medium) was added and incubated at 37 °C for 2 h. Absorbance values were measured at 450 nm using an enzyme meter (Bio-Rad, Japan).

2.2.2. Live-dead cell staining by Calcein-AM/PI

Calcein-AM specifically labels live cells and PI specifically labels dead cells.Brain tumor cells from different treatment groups were washed, digested, collected and centrifuged, then washed twice with 1 × Assay Buffer and centrifuged until the supernatant was colorless. Cells from each treatment group were resuspended with 100 μL of Buffer containing staining solution (Calcein-AM concentration = 2.0, PI concentration = 4.5) and then placed onto a cell crawler plate inside a 6-well plate, and incubated for 30 min at room temperature, then discarded the staining solution and sealed with anti-fluorescent attenuator. After incubation for 30 min, the staining solution was discarded, and the plate was sealed by adding anti-fluorescence attenuator, and then observed under a fluorescence microscope in a dark environment, and three fields of view were randomly selected in each group for taking pictures.

2.2.3. Cell migration assay by wound healing

U87 and U–CH1 cells were inoculated into 6-well plates and treated in groups when the cell density was appropriate. After that, the tip of 10 μL pipette tip was used for scratch, and then the cells were washed with PBS three times to remove the exfoliated cells in the well plate as far as possible. The scratch edge was observed and recorded under an inverted microscope (Olympus, CKX53). After the cells were placed in the incubator for 24 h, the scratch area was recorded under the microscope again. The scratch area was calculated using Image J software.

2.2.4. Evaluation of invasion assays by cell transwells

The invasive ability of each group of brain tumor cells was evaluated using a Transwell device (8.0 μm, Coming, USA). After the cells were grouped and processed, cells with a density of 2×10^5/mL (200 μL) were inoculated in the upper chamber with serum-free DMEM. DMEM (500 μL) containing 10 % FBS was placed in the lower chamber (to direct the invasion of U87, U–CH1 cells by serum concentration gradient). After incubation for 24 h, the old medium was discarded, and the cells were fixed with 4 % paraformaldehyde for 20 min at 37 °C, and then stained with crystal violet (0.4 %) for 15 min. The filters were carefully removed, and the excess of crystal violet staining solution was removed from the filters by gently washing with PBS. Observation was performed using an inverted microscope (Olympus, Japan), and three fields of view were randomly selected from each group for photographing. The number of cells passed through the filter membrane was counted using Image J software.

2.2.5. Apoptosis of tumor cells was detected by Annexin V-FITC/PI double staining

The cell wells of U87 and U–CH1 were inoculated into 6-well plates with 2×10^5 cells per well, and when the cells were completely adhered to the wall, they were grouped and treated, and then digested with EDTA-free trypsin and collected the cells in each group after 4 h. Cells were collected by centrifugation for 5 min with a bench-top freezing centrifuge (Eppendorf, Germany) at 4 °C, 1000 rpm. Trypsin digestion time should not be too long to prevent false positives. Cells were washed twice with pre-cooled PBS, each time at 4 °C, 1000 rpm, and centrifuged for 5 min to collect cells. Cells were resuspended with 100 μL of 1 × Binding Buffer, 5 μL of Annexin V-FITC and 5 μL of PI reagent were added, gently blown and mixed, and the reaction was carried out for 20 min at room temperature, protected from light, then 400 μL of 1 × Binding Buffer was added, mixed, and placed on ice, and the samples were detected by flow cytometry (BD Biosciencesgon, USA) within 1 h.

2.2.6. Western-blotting detection of Caspase-3 expression

Proteins were extracted from U87 cells after treating the cells with RIPA buffer (containing 1 % PMSF). The protein samples were denatured at high temperature and separated by electrophoresis on a 10 % SDS-PAGE gel. The blot was closed and incubated with anti-Caspase-3 antibodies (1:1000), at 4 °C overnight. After the buffer was thoroughly rinsed, the blot was incubated with secondary antibody (1:10,000, CST, USA) for 1 h at 37 °C. Membranes were scanned using a multifunctional chemiluminescence imager (analytik jena, Germany). Protein blot analysis was performed using Image J software.

2.2.7. Establishment of a murine model of brain tumor xenograft and pathological changes

All animal experiments were approved by the Animal Care and Ethics Committee of Guilin Medical College. Female BALB/c nude

mice (4 weeks old, weighing 18–20 g) were purchased from Hunan Slaughter Kingda Laboratory Animal Co. U87 and U–CH1 cells of logarithmic growth phase were harvested 1×10^6 each respectively, washed, and then the cells were resuspended with 100/μL of DMEM without double antibody, and injected subcutaneously into the right dorsal side of the mice with a syringe. When the tumor diameter was about 5 mm, the hormonal mice were randomly divided into 3 groups for further experiments.

2.2.8. Treatment of subcutaneous tumors

Mice were anesthetized with 2.5 % isoflurane, and 15 mg of UCNPs@mSiO$_2$-NH$_2$&RBS was administered intratumorally per 100 g of body weight, and kept under light protection for 24 h. The rest of the ruffed mice were treated with complete protection from light, except for the tumor body. The light power was 2.0 W and the energy density was 150 J/cm^2. The experimental groupings (n = 5 for each group) were as follows: (1) Control group: injection of equal volume of saline only; (2) UCNPs@mSiO$_2$-NH$_2$&RBS group: intratumor injection only (UCNPs@mSiO$_2$-NH$_2$&RBS, 15 mg/100g); (3) NIR + UCNPs@mSiO$_2$-NH$_2$&RBS group: Intratumor injection of UCNPs@mSiO$_2$-NH$_2$&RBS (15 mg/100g), 24h after injection with 808 nm laser irradiation of the tumor site only, Laser energy density 150 kJ/cm^2, irradiation duration 10 min, avoiding the light feeding for 24 h for the next cycle of treatment, a total of three treatment cycles. All model mice received 3 consecutive cycles of treatment, and after 7 days the mice were killed by cervical dislocation and the tumors were sampled. Mice were euthanized if their body weight met the preset criteria of 10 % over the starting body weight or paralysis.

2.2.9. Tumor volume, mouse weight

Tumor volume was measured daily after treatment and mice body weight was monitored for a total of 7 observations. Tumors were excised at the end of treatment and tumor volume was calculated using the following formula: volume = length × width^2 × 0.5.

2.2.10. Pathologic changes and expression of Ki67

Tumor samples were fixed in 4 % paraformaldehyde overnight, tissue was dehydrated and embedded in paraffin, and sectioned (5 μm). Routine pathology was performed with hematoxylin and eosin (H&E) staining. Immunohistochemistry (IHC) was performed to detect Ki67 expression in tumors, paraffin sections of tumors were deparaffinized for hydration, endogenous peroxidase activity was blocked using 3 % hydrogen peroxide, and the sections were incubated with anti-Ki67 overnight at 4 °C, and HRP-labeled secondary antibody (CST, USA) was incubated with the sections for 60 min. Next, samples were incubated with diaminobenzidine for 10 min, restained with hematoxylin, dehydrated and covered with coverslips. Sections were observed using a microscope (Olympus, Japan), and immunoreactive signals were quantified using Image J software.

2.3. Statistical analysis

The statistical software SPSS 24.0 and the software GraphPad Prism 8.0 were used for data analysis and graphing, and all experiments were repeated at least three times, and the data were expressed as mean ± standard error (mean ± SEM), and the one-way ANOVA was used for comparing multiple groups, and the difference was taken to be statistically significant at $p < 0.05$ Significance.
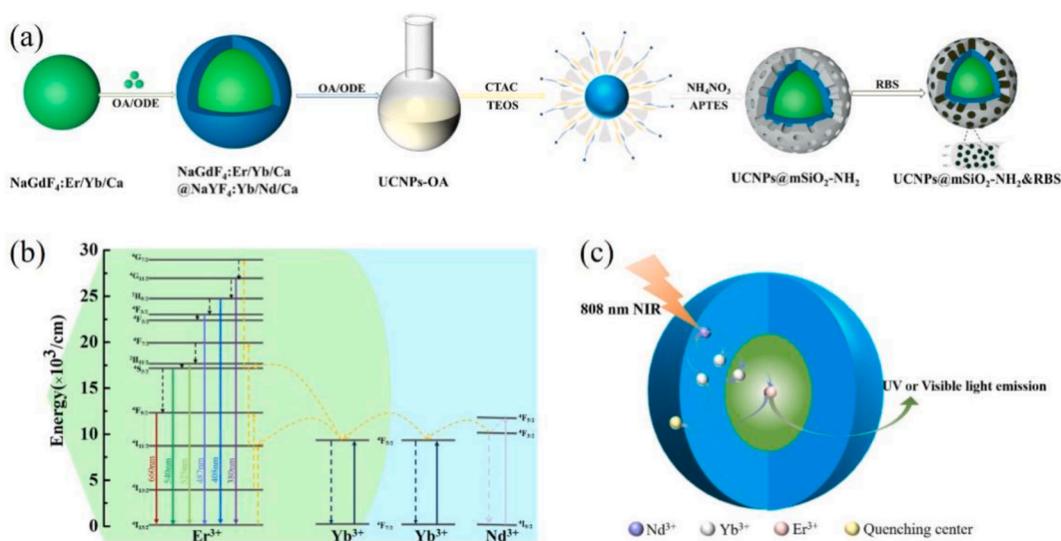

Fig. 1. (a) Synthesis scheme of UCNPs@mSiO$_2$-NH$_2$&RBS, (b, c) Schematic diagrams of conversion emission and energy transfer mechanism on CS UCNPs.

3. Results and discussion

3.1. Morphology, structure, and fluorescence properties of UCNPs@mSiO$_2$

The synthesis of the photocontrolled NO release platform, based on the principle of energy resonance transfer, is schematically shown in Fig. 1(C). UCNPs and CS UCNPs were synthesized using the thermal decomposition method. The optimal ratio of UCNPs fluorescence intensity was achieved by adjusting the concentration of doped ions. The hydrothermal surface coating of CS UCNPS was carried out with mesoporous silica for loading photosensitive NO donors.

The luminescence principle of UCNPs is shown in Fig. 1(b). When excited by 808 nm NIR light, the 808 nm photon energy is absorbed by the shell sensitizer Nd^{3+}. This absorption causes the electrons in the ground state of ^{4}I$_{9/2}$ of Nd^{3+} to transition to the ^{4}F$_{5/2}$ energy level. However, the ^{4}F$_{5/2}$ energy level subsequently undergoes the radiation-free relaxation to the ^{4}F$_{3/2}$ energy level. The energy is then transferred to Yb^{3+} in the shell layer, resulting in the transition of the ground state ^{4}F$_{7/2}$ of Yb^{3+} to the ^{4}F$_{5/2}$ excited state. Yb^{3+} in the nucleus shell plays an important role in the energy migration on the conversion mobilizer part. Yb^{3+} in the nucleus finally transfers the energy to the intermediate excited state energy level of Er^{3+} through ET. When Er^{3+} receives the transferred energy from Yb^{3+}, it transitions from the ^{4}S$_{3/2}$ energy level to ^{4}G$_{7/2}$. The excited state energy level becomes unstable, leading to radiationless relaxation to the ^{4}G$_{11/2}$ state, with a part of the energy jumping to the ground state ^{4}I1$_{5/2}$. This process results in the formation of the emission peak of violet light emission at 380 nm. After another portion of the energy in the ^{4}G$_{11/2}$ state undergoes radiationless transition to the ^{2}H$_{9/2}$ state, a portion of it is radiated to the ground state ^{4}I$_{15/2}$, resulting in 408 nm blue light emission. The energy located in the ^{2}H$_{9/2}$ state undergoes another segment of radiationless relaxation to ^{4}H$_{3/2}$, and then the part of the energy returns to the ground state ^{4}I$_{15/2}$, forming 487 nm blue-violet emission. Er^{3+} then absorbs energy from Yb^{3+} in the nucleus and passes to the intermediate excited state ^{4}I$_{11/2}$ energy level of Er^{3+} through ET from the excited state ^{4}F$_{5/2}$ of Yb^{3+}. It causes the electrons in this energy level to gain enough energy to jump to the ^{4}F$_{7/2}$ energy level. The ^{4}F$_{7/2}$ energy level, being unstable, undergoes radiationless relaxation to the ^{2}H$_{11/2}$ energy level, and a part of the energy in the ^{2}H$_{11/2}$ energy level undergoes radiationless relaxation to the ^{4}S$_{3/2}$ energy level, while another part directly returns to the base state ^{4}I$_{15/2}$ energy level. The emission from these processes results in the green luminescence at 525 nm and 540 nm. The other part of the energy in the ^{4}S$_{3/2}$ energy level then undergoes radiative decay either directly to the ^{4}I$_{15/2}$ energy level of the ground state after a radiationless leap to ^{4}F$_{9/2}$ or the energy absorbed from the intermediate state of ^{4}I$_{13/2}$ is directly returned to the ^{4}I$_{15/2}$ energy level of the ground state after an energy-leap to ^{4}F$_{9/2}$, resulting in the red light emission at 660 nm.

As shown in Fig. 1(c), when irradiated by 808 nm NIR, Nd^{3+} in the shell layer absorbs the photon energy of 808 nm NIR light. Yb^{3+} transfers photon energy to Nd^{3+} in the shell layer through the bridging effect of doped Yb^{3+} in the core and shell. Finally, Yb^{3+} in the nucleus transfers the energy to the light-emitting center Er^{3+}, facilitating an effective Nd^{3+}-Er^{3+} energy conversion. However, Yb^{3+} in the shell layer may also transfer the absorbed energy to the burst center on the surface of UCNPs, such as the surface of the oleic acid ligand or solvent molecules, etc. Therefore, the luminescence center can transfer the energy to the surface of the burst center, resulting in fluorescence quenching and weakening the upconversion luminescence.

Energy resonance transfer is based on the energy transfer between two chromophores in Fig. 2. When energy resonance transfer takes place, the excited donor transfersits energy to the acceptor. This is indicated by a reduction in the fluorescence emission intensity of the donor molecule and an enhancement in the fluorescence of the acceptor. The donor undergoes non-radiatively relaxation of the energy from the excited state to the ground state, while the acceptor receives the energy and becomes excited to the excited state.

Two conditions are required for the Förster energy resonance transfer to occur: (1) the distance between the donor and acceptor molecules needs to be less than 10 nm, and (2) the emission spectrum of the donor molecule has an overlapping part with the absorption spectrum of the acceptor molecule. This can be simply described by the following equation:

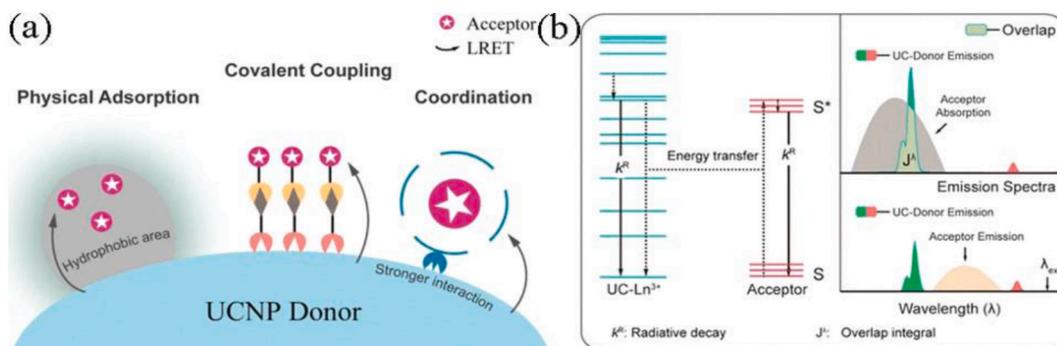$$E_{FRET} = \frac{R_0^6}{R_0^6 + r^6} \qquad (1)$$

Fig. 2. Schematic diagram of energy resonance transfer principle.

$$R_0^6 = \frac{9(In10)\kappa^2\Phi_D J}{128\pi^5 n^4 N_4} \tag{2}$$

Where, E_{FRET}——Efficiency of FRET;

R_0——Foster distance;

r——Donor-acceptor distance;

κ^2——orientation factor;

Φ_D——Quantum yield of donor fluorescence;

N——refractive index;

J——Overlap integration between donor and recipient.

The crystal morphology and particle size of UCNPs are shown in Fig. 3(a、d). Both C UCNPs and CS UCNPs displayed a highly homogeneous hexagonal morphology, well-defined boundaries, and homogeneous particle sizes on ultrathin carbon mesh. C UCNPs and CS UCNPs revealed average particle sizes of 11.7 ± 0.75 nm and 21.03 ± 1.36 nm, respectively as shown in Fig. 3(c、f). Both C UCNPs and CS UCNPs showed well-defined crystal spacing when studied under HRTEM for fig (b、e). Using Bragg's equation: $n\lambda = 2d\sin\theta$, and the angular values of the diffraction peaks of NaGdF$_4$ (110) and NaYF$_4$ (110), the crystalline facet spacing for the NaGdF$_4$ (110 was calculated as 0.29 nm. The CS UCNPs crystal plane spacing was found to be 0.52 nm, which is in good agreement with the angular values of NaGdF$_4$ (110) and NaYF$_4$ (110) diffraction peaks. These findings indicate that the synthesized UCNPs display excellent crystalline properties.

The morphology of UCNPs@mSiO$_2$, formed by using CTAC as a templating agent and NaOH as a catalyst, is shown in Fig. 3(g). The morphology shows that the core-shell nanoparticles are uniformly encapsulated by mesoporous silica, showing a mesoporous structure. The particle size analysis shows that the water and kinetic diameter of UCNPs@mSiO$_2$ was about 43.842.19 nm, and the thickness of mesoporous silica was about 7.5 nm as shown in Fig. 3(h) and Equ(1、2). These results provide a strong base for the next energy resonance transfer.

Fig. 4(a) shows the IR analysis of UCNPs and UCNPs@mSiO$_2$. The characteristic peaks of hydroxyl (3430 cm^{-1}), carbon-oxygen double bond (1566 cm^{-1}), and carbon-carbon double bond (1631 cm^{-1}) in the methylene group (2921 cm^{-1} and 2858 cm^{-1}) and carboxyl group can be observed. A significant reduction in the intensities of the methylene characteristic peaks, carbon-oxygen double bond, and carbon-carbon double was observed after the coating of mesoporous silica. New prominent characteristic peaks such as the asymmetric and symmetric broader and stronger telescopic vibrational peaks of Si–O–Si (1090 cm^{-1} and 796 cm^{-1}), and the telescopic vibrational peaks of Si–OH (965 cm^{-1}), which are the characteristic peaks of the absorption of siliceous materials, also appeared. The
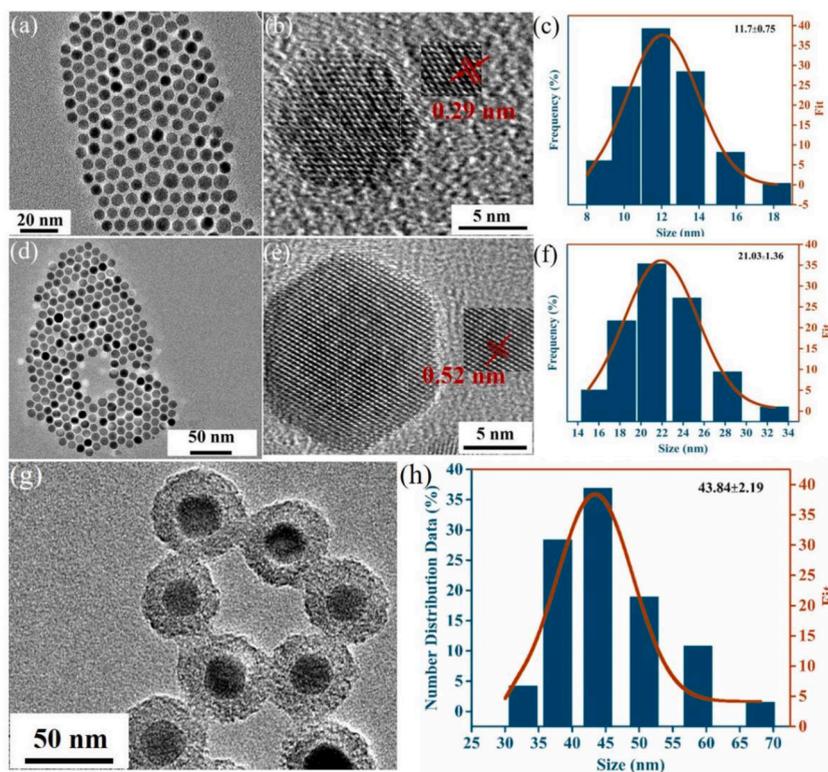

Fig. 3. (a) TEM image, (b) HRTEM and (c) particle size distribution of C UCNPs; (d) TEM image, (e) HRTEM image and (f) particle size distribution of CS UCNPs; (g) TEM image and (h) particle size distribution of UCNPs@mSiO$_2$
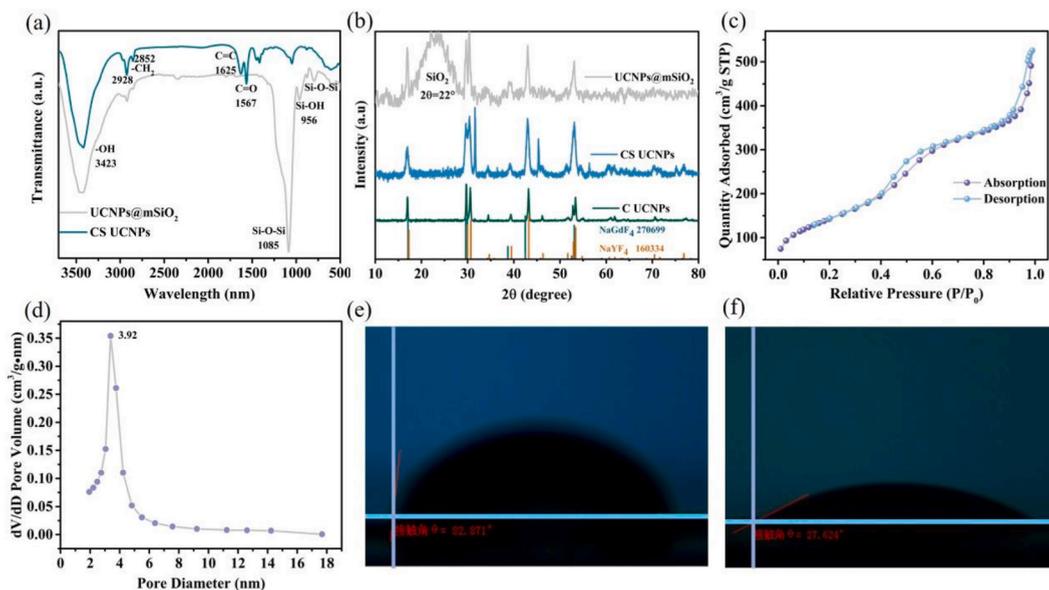
Fig. 4. (a) The FT-IR spectra of CS UCNPs、UCNPs@mSiO$_2$, (b) XRD spectra of C UCNPs、CS UCNPs and UCNPs@mSiO$_2$, (c) N$_2$ adsorption and desorption isotherms, (d) Pore size distribution curves of UCNPs@mSiO$_2$), Contact angle diagram of (e) CS UCNPs, (f) UCNPs@mSiO$_2$

results of the XRD analysis of UCNPs and UCNPs@mSiO$_2$ are shown in the figure. Fig. 4(b). The XRD peaks of C UCNP and CS UCNPs were found sharp and prominent with clear baselines, indicating a high degree of crystallinity. The intensity of the diffraction peaks decreased after coating with mesoporous silica, however, the main characteristic diffraction peaks of CS UCNPs were still retained. Similarly, the encapsulated peaks of silica appeared at $2\theta = 22°$. The characteristic peaks of the inclusion pattern indicate that the silica possesses an amorphous structure with extensive reflections. This demonstrates that mesoporous silica was successfully coated on the surface of UCNPs and did not affect the crystalline structure of the core-shell structure. FR-IR and XRD analyses together demonstrate the successful coating of mesoporous silica on the surface of UCNPs.

Fig. 4(c) shows the adsorption-desorption isotherm of N$_2$, providing insights into the mesoporous properties of UCNPs@mSiO$_2$. The figure shows a type IV isotherm, indicating a strong force on N$_2$ under low-pressure conditions. Further, an H1-type hysteresis loop appeared in the middle section of the curve, indicating a mesoporous structure resembling a tubular cylinder with openings at both ends, meeting the requirements for drug loading. The analysis showed a specific surface area of the mesopore as 521.756 m^2 g^{-1}, the pore volume as 0.8940 cm^{-3} g^{-1}, and the pore size as 3.95 nm as shown in Fig. 4(d). The contact angle analysis was carried out for UCNPs and UCNPs@mSiO$_2$ to characterize the transformation of hydrophobicity to hydrophilicity on the surface of UCNPs due to mesoporous silica. As shown in Fig. 4(e, f), the contact angle of UCNPs was 82.87 while the mesoporous silica-coated UCNPs displayed a reduced contact angle of 27.674°, indicating improved hydrophilicity. This improvement in the hydrophobicity suggests good biocompatibility for UCNPs, thus providing a basis for its application in biological experiments for constructing a photocontrol platform.

Fig. 5(a) shows the fluorescence properties of C UCNPs, CS UCNPs, and UCNPs@mSiO$_2$. From the figure, it can be seen that the fluorescence intensity of UCNPs@mSiO$_2$ was observed to decrease compared to that of CS UCNPs, however, the extent of the decrease was minor, and it remained significantly higher than that of C UCNPs. At the main emission peaks of 525 nm and 540 nm, the fluorescence intensity of UCNPs@mSiO$_2$ was observed to be 8 times higher than that of C UCNPs. Therefore, the mesoporous silica had
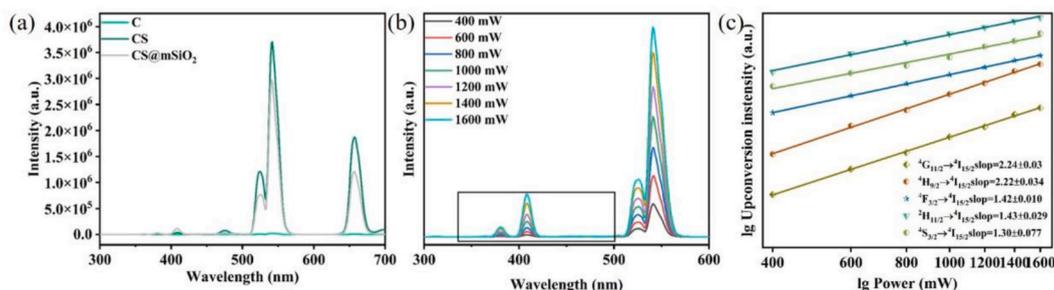

Fig. 5. (a) Trend plot of fluorescence intensity of C UCNPs, CS UCNPs, and UCNPs@mSiO$_2$, (b) Fluorescence spectra of CS UCNPs with different power excitation, (c) Logarithmic plot of the intensity of each multiphoton process of CS UCNPs versus the increase of excitation light power.

a minimal effect on the fluorescence performance of UCNPs. Therefore, mesoporous silica is an effective material for high-quality surface modification. It can change the surface of UCNPs from lipophilic to hydrophilic, ensuring their good dispersion and biocompatibility. Moreover, it has minimal effects on fluorescence performance, providing a solid base for photo-control release of NO.

The variation between nanoparticle luminescence intensity and excitation power was shown in Equation. (3):

$$I \propto P^n \tag{3}$$

Where, P—Excitation power,

I— Up-converted luminous intensity,

n—Number of photons that excite up-conversion luminescence.

In the equation, "n" represents the number of pump photons in the excited photoemission state, providing insights into the nature of multiphoton emission. The relationship between power and upconversion luminescence intensity is depicted in a double logarithmic plot as shown in Fig. 5(b、c). A linear fit yielded a slope of 2.24 at the emission peak of 380 nm, 2.22 at the emission peak of 410 nm, 1.42 at the emission peak of 487 nm, 1.43 at the emission peak of 525 nm, and 1.30 at the emission peak of 540 nm. Wittke et al. [26] proposed a power of 3/2 of the excitation and emission law, signifying a process involving the production of two emission photons from three absorption photons. This demonstrates that the upconversion emission of Er^{3+} is a two-photon process. The slopes at 487 nm, 525 nm, and 540 nm being less than 2 are attributed to the synergistic energy transfer and cross-relaxation.

It is clear from XRD and fluorescence patterns that Ca^{2+} doping can affect the crystalline properties of C UCNPs and CS UCNPs, thereby increasing the intensity of upconversion emission. To further investigate the effects of Ca^{2+} doping on the fluorescence lifetimes of C UCNPs and CS UCNPs, the lifetimes of the main emission peaks at 525 nm and 540 nm (corresponding to $^4S_{3/2} \rightarrow {^4I_{15/2}}$ and $^4H_{11/2} \rightarrow {^4I_{15/2}}$ radiative leaps) in CS UCNPs were studied. Fig. 6(a–d) shows the luminescence decay curves of C UCNPs and CS UCNPs at 525 nm and 540 nm energy level jumps. The decay lifetime (τ) was fitted in the graph as shown in Fig. 6, and the results showed that the fluorescence lifetime was significantly prolonged with the increase in Ca^{2+} doping. According to the theory of fluorescence dynamics, the formula for calculating the energy level lifetime is shown in (4) [27].

$$\tau = 1 / (\Gamma + k_{nr}) \tag{4}$$

Where, τ — Decay lifetime,

Γ — Up-converted luminous intensity,

k_{nr} — Nonradiative decay rate.

In equ.4, Ca^{2+} doping reduces the symmetry of localized crystals around lanthanide ions, resulting in a decrease in the radiation attenuation rate (K_f), and thereby, an effective increase in the fluorescence lifetime. Therefore, the fluorescence lifetime of CS UCNPs
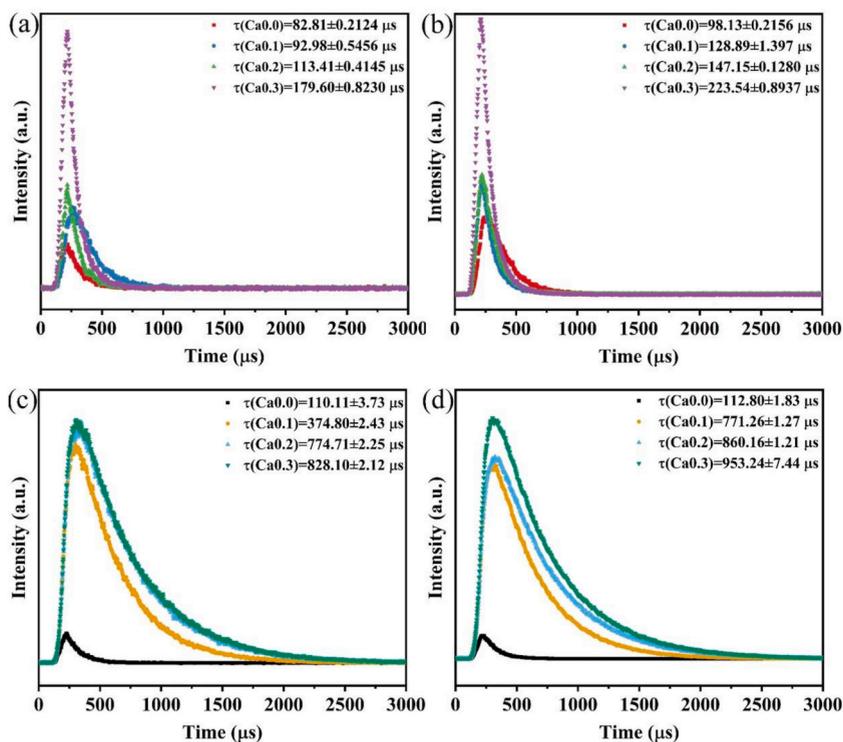

Fig. 6. Attenuation curves of (a, b) C UCNPs, (c, d) CS UCNPs at 525 nm and 540 nm with different doping concentrations of Ca^{2+}.

was found longer than that of C UCNPs. The mechanism behind this is that Ca^{2+} doping and core-shell strategy expand the acceptance area of UCNPs in NIR light, and protect the luminous center of the nucleus. This, in turn, reduces the influence of cross-relaxation and non-radiative transition, thus leading to a decrease in the non-radiative decay rate K_{nr}.

3.2. Loading the RuNO-Thnl into UCNPs@mSiO$_2$

The zeta potentials of UCNPs, UCNPs@mSiO$_2$, UCNPs@mSiO$_2$-NH$_2$, RBS, and UCNPs@mSiO$_2$-NH$_2$&RBS were investigated and the results are shown in Fig. 7(a). The surface of UCNPs was found almost uncharged, while UCNPs@mSiO$_2$ displayed negatively charged surfaces. In the process of mesoporous silica formation, tetraethyl orthosilicate forms a large number of Si–O–Si bonds after hydrolysis or condensation. These Si–O–Si bonds form hydrogen bonds with hydrogen ions in water molecules, leading to the generation of a large number of OH^- ions. Therefore, the surface of mesoporous silica coated with nanoparticles showed a negative charge. As shown in the figure, RBS also exhibited a negative charge. RBS undergoes an ionization reaction in an aqueous solution to produce NH_4^+ and $Fe_2S_2(NO)_2^{2-}$. NH_4^+ ions undergo a weaker hydrolysis reaction with water to produce less H^+. Therefore, RBS displayed a weak negative electronegativity.

The iron-sulfur nitroso compound RBS was loaded into mesoporous silica, and the photocontrolled NO release platform of UCNPs@mSiO$_2$-NH$_2$&RBS was successfully constructed. As shown in Fig. 7(b), the characteristic peaks of nitroso (-NO$_2$) were observed at a wave number of 1740 cm^{-1}. Similarly, the characteristic peaks of –NH$_2$ and Si–O–Si were also observed, indicating the successful loading of RBS on UCNPs@mSiO$_2$-NH$_2$. Fig. 7(c) shows the UV absorption spectra of UCNPs@mSiO$_2$-NH$_2$, RBS, and UCNPs@mSiO$_2$-NH$_2$&RBS. RBS and UCNPs@mSiO$_2$-NH$_2$&RBS showed similar and broad absorption bands at 300–600 nm. However, UCNPs@mSiO$_2$-NH$_2$ without drug loading showed a clear absorption band for NO in the ultraviolet region. Therefore, the successful loading of photosensitive NO donors can be confirmed through both infrared and ultraviolet images.

The loading capacity of UCNPs@mSiO$_2$-NH$_2$&RBS was determined through thermogravimetric analysis (TGA) and ultraviolet spectroscopy. As shown in Fig. 8(d), the weight loss difference between UCNPs@mSiO$_2$-NH$_2$ and UCNPs@mSiO$_2$-NH$_2$&RBS was found to be 21.52 %, with a weight loss of 2.77 mg for both samples. The loading, calculated as 0.6183 mg, corresponds to 88.33 % of the loading rate of RBS. Further, UV spectroscopy was performed to validate the RBS loading. The UV absorption spectra of RBS with different concentrations (4.5×10^{-4}, 3×10^{-4}, 2×10^{-4}, 1×10^{-4}, 5×10^{-5}, 2.5×10^{-5} mol/L) were plotted for validation. According to Lombard-Behr's law, the absorbance of incident light irradiating a vertically oriented, uniform, non-scattering system is proportional to both the concentration of the absorbing substance and the thickness of the absorbing layer. Fig. 8(a–c) shows the standard curve of the absorbance of different concentrations of RBS fitted to the concentration at the same absorption wavelength (400 nm was selected). The fitting results in an R^2 value of 0.9949, indicating a strong linear relationship between the concentration of RBS and UV absorbance.

3.3. NIR-induced NO release and kinetic analysis of UCNPs@mSiO$_2$-NH$_2$&RBS

Förster energy resonance transfer (FRET) refers to a non-radiative energy transfer between two chromophores. Moreover, the efficiency of energy resonance transfer not only depends on the distance between the donor and the acceptor but also the degree of overlap between the fluorescence spectrum of the donor and the absorption spectrum of the acceptor in equ.2. Therefore, to investigate the potential for NO release via energy resonance transfer, the fluorescence spectra of C UCNPs, CS UCNPs, and UCNPs@mSiO$_2$, along with the UV spectra of RBS were analyzed.

As shown in Fig. 9(b), RBS displayed a broad absorption band in the range of 300–600 nm, and the emission peaks of the luminescence center Er appeared at 380, 410, 487, 525, and 540 nm, respectively. Interestingly, the UV absorption bands of RBS demonstrated a high degree of overlap with those of UCNPs. The energy resonance transfer between UCNPs@mSiO$_2$ and RBS occurs due to large spectral overlaps and short donor-acceptor molecular distances. As shown in Fig. 9(a), the mechanism involves the absorption of 808 nm NIR by the upconversion nanoparticles, which then transfer their energy to the luminescence center through upconversion, resulting in UV or visible light emission. The energy is then transferred to the photosensitive NO donor RBS through
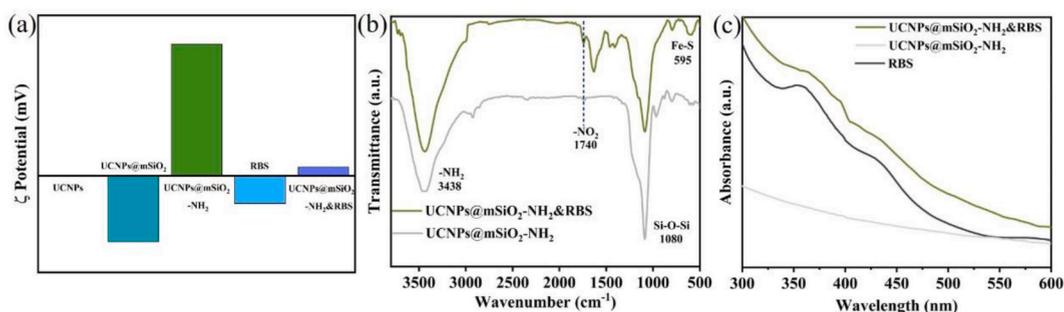

Fig. 7. (a) Zeta potential analysis of UCNPs, UCNPs@mSiO$_2$, UCNPs@mSiO$_2$-NH$_2$, RBS and UCNPs@mSiO$_2$-NH$_2$&RBS; (b) IR spectra of UCNPs@mSiO$_2$-NH$_2$, UCNPs@mSiO$_2$-NH$_2$&RBS; (c) UV spectra of UCNPs@mSiO$_2$-NH$_2$, RBS and (c) UV spectroscopy of UCNPs@mSiO$_2$-NH$_2$&RBS
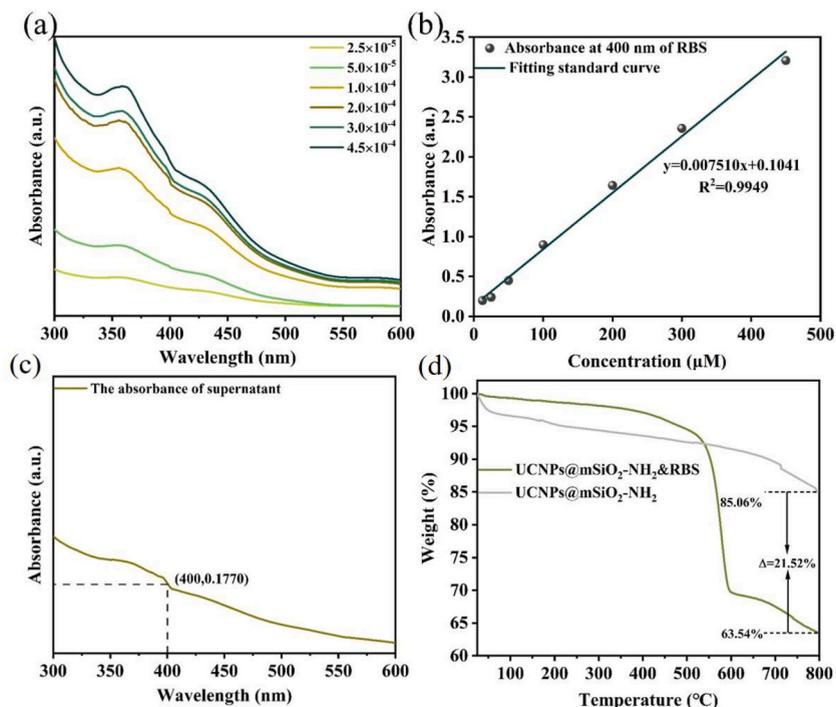
Fig. 8. (a) UV absorption spectra of different concentrations of RBS, (b) standard curve fitted with absorbance at 400 nm, (c) UV absorption spectra of the supernatant of UCNPs@mSiO$_2$-NH$_2$&RBS, (d) thermogravimetric curves of UCNPs@mSiO$_2$-NH$_2$ and UCNPs@mSiO$_2$-NH$_2$&RBS
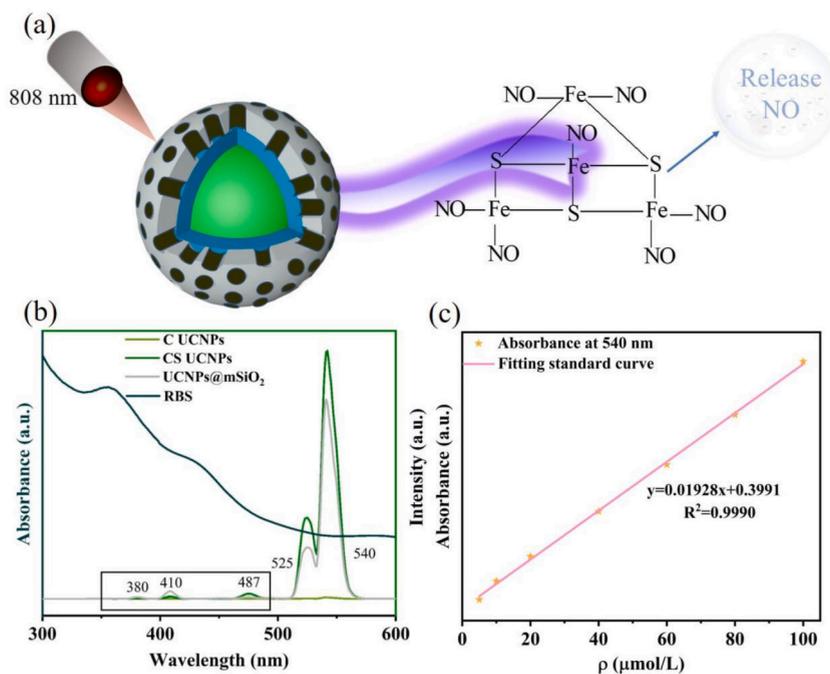

Fig. 9. (a) Schematic diagram of NO release by 808 nm excitation of UCNPs@mSiO$_2$-NH$_2$&RBS, (b) Fluorescence spectra of C UCNPs, CS UCNPs, UCNPs@mSiO$_2$, and UV absorption spectra of RBS, (c) Fitted standard curve of NO concentration.

energy resonance transfer, allowing the RBS to obtain the energy and then release NO.

In an aqueous solution or *in vivo*, NO undergoes rapid oxidation and forms NO$_2^-$. The Griess reagent reacts with NO$_2^-$ in a colori-metric manner, displaying a linear correlation between the concentration of the product and NO$_2^-$. This reaction shows a UV peak at

540 nm, enabling the determination of the concentration of NO released based on the relationship between absorbance and concentration of NO_2^-. A standard curve of absorbance versus NO_2^- concentration was fitted as shown in Fig. 9(c), The R^2 value of the fitted curve was 0.9990, indicating a strong linear relationship between absorbance and nitrite ions.

The 808 nm excitation of UCNPs@mSiO$_2$-NH$_2$&RBS resulted in a discoloration of the solution when treated with a Griess reagent. The discoloration of the Griess reagent and the absorption peak at 540 nm in the UV spectrophotometer of the reacted solution confirm the NO production. This provides evidence supporting the occurrence of energy resonance transfer in the UCNPs@mSiO$_2$-NH$_2$& RBS. The NO release kinetics were analyzed based on the power of the NIR light exciter (1.0 W, 1.5 W, 2.0 W), the irradiation time of the NIR light (5 min, 10 min, 15 min, 20 min) and the concentration of UCNPs@mSiO$_2$-NH$_2$&RBS (1.25 mg/mL, 1.0 mg/mL, 0.5 mg/mL, 0.25 mg/mL) and the results are shown in Fig. 10. The concentration of the NO released was plotted versus the concentration of UCNPs@mSiO$_2$-NH$_2$&RBS, the excitation light power and irradiation time trend, which are depicted based on the change in solution color as shown in the inset of Fig. 10. It is evident from the observed chromogenic reaction between NO and the Griess reagent that FRET has successfully occurred between the UCNPs and the RBS. The figure shows that the color peak of NO_2^- at 540 nm increases with the concentration of UCNPs@mSiO$_2$-NH$_2$&RBS, indicating that the release of NO also increases with the concentration. Similarly, it can be obtained that the increase in the irradiation time and exciter power of NIR light increases the absorbance of NO_2^- at 540 nm, then it is proved that the release of NO increases with it. In conclusion, the concentration of UCNPs@mSiO$_2$-NH$_2$&RBS, the power of the exciter, and the time of NIR light irradiation are all important parameters affecting the release of NO. In the case where the concentration of UCNPs@mSiO$_2$-NH$_2$&RBS was 1.25 mg/mL with 5 min of irradiation at an excitation power of 1.0 W, the released NO was 0.051 mM. Further, at a concentration of 0.25 mg/mL with 20 min of irradiation and an excitation power of 1.0 W, the released NO was 0.0068 mM. These concentrations are all within the range of 1 μM-1 mM, indicating their potential anti-tumor effects.

4. NO toxicity assessment and releasing

4.1. Cytological evaluation of 808 nm NIR-excited UCNPs@mSiO$_2$-NH$_2$&RBS

4.1.1. Characterization of the cytotoxic effects of 808 nm NIR-excited UCNPs@mSiO$_2$-NH$_2$&RBS using the CCK-8 assay

Zhao et al. [28] constructed Ca^{2+}-doped upconversion nanoparticles that released NO under 980 nm excitation, which resulted in a significant decrease in the viability of HeLa cells by MTT assay. In order to verify the cytotoxic effect of UCNPs@mSiO$_2$-NH$_2$&RBS under 808 nm excitation, the cytotoxicity and biocompatibility were investigated by exposing U87 and U–CH1 cells to UCNPs@mSiO$_2$-NH$_2$, RBS, and UCNPs@mSiO$_2$-NH$_2$&RBS treatments with or without 808 nm NIR irradiation. The UCNPs@mSiO$_2$-NH$_2$&RBS
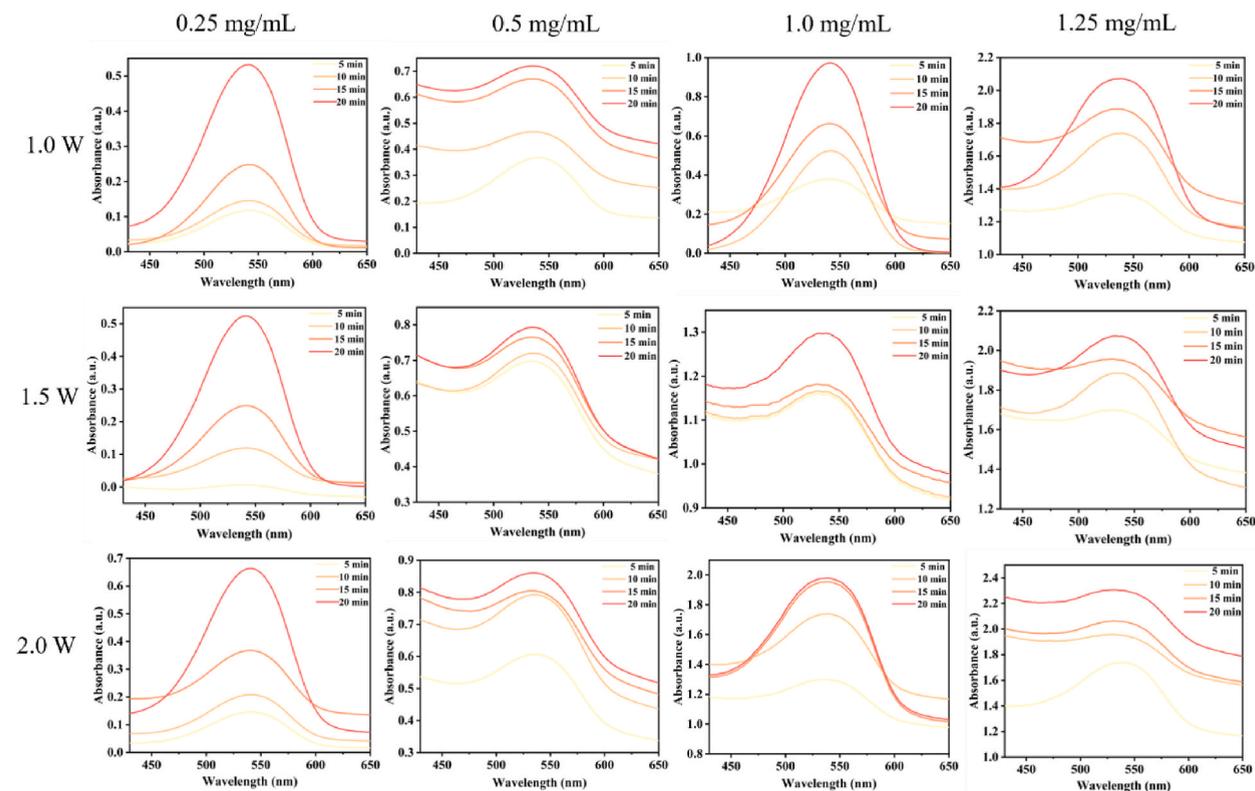

Fig. 10. Effects of different excitation powers (1.0 W, 1.5 W, 2.0 W), light times (5 min, 10 min, 15 min, 20 min) and concentrations of UCNPs@mSiO$_2$-NH$_2$&RBS (1.25 mg/mL, 1.0 mg/mL, 0.5 mg/mL, 0.25 mg/mL) on the release of NO.

concentration causing 50 % inhibition (IC$_{50}$) under 808 nm NIR excitation was determined. Fig. 11(a) shows that, in the absence of 808 nm NIR irradiation, when the concentrations of both UCNPs@mSiO$_2$-NH$_2$ and UCNPs@mSiO$_2$-NH$_2$&RBS were 0.35 mg/mL, the OD value of UCNPs@mSiO$_2$-NH$_2$ for U87 cells was found to be 90.7 %. The OD value for U87 cells treated with UCNPs@mSiO$_2$-NH$_2$&RBS was found to be 88.3 %. Fig. 11(d) shows that when the concentrations of both UCNPs@mSiO$_2$-NH$_2$ and UCNPs@mSiO$_2$-NH$_2$&RBS were 1.0 mg/mL, OD values of U–CH1 cells were close to 100 %, indicating low cytotoxicity to U87 and U–CH1 cells. As shown in Fig. 11(b), upon 808 nm NIR irradiation of UCNPs@mSiO$_2$-NH$_2$ and UCNPs@mSiO$_2$-NH$_2$&RBS, the OD values for U87 cells treated with 808 nm NIR-excited UCNPs@mSiO$_2$-NH$_2$ group were almost unchanged compared to the cases without 808 nm NIR irradiation. However, in the 808 nm NIR-excited U87 cells treated with UCNPs@mSiO$_2$-NH$_2$&RBS group, the activity of U87 cells gradually decreased with the increase in UCNPs@mSiO$_2$-NH$_2$&RBS concentration. When the concentration of UCNPs@mSiO$_2$-NH$_2$&RBS was 0.3 mg/mL, the OD value of U87 cells was about 50 %, representing the IC$_{50}$ value of glioma cells. Similarly, Fig. 11(e) shows that the activity of chordoma cells treated with UCNPs@mSiO$_2$-NH$_2$&RBS under 808 nm NIR irradiation at a concentration of 0.8 mg/mL was 50 %, representing the IC$_{50}$ value of chordoma cells. It indicates that UCNPs@mSiO$_2$-NH$_2$&RBS can be stimulated to release a large amount of NO in the presence of 808 nm NIR, thus inhibiting the activity of U87 and U–CH1 cells. The subsequent experiments of cell migration and invasion, live/dead cell staining, Hoechst staining, and cell flow were carried out based on this concentration.

As shown in Fig. 11(c), at a concentration of 0.021 mg/mL of RBS, the OD value of U87 cells was 90.97 %, thus indicating lower cytotoxicity. Similarly, at the same concentration of RBS in the presence of NIR, it had a lesser effect on the activity of glioma cells. Fig. 11(f) shows that when in the presence or absence of NIR irradiation, the OD values of U–CH1 cells treated with 0.06 mg/mL concentration of RBS were close to 100 %. Therefore, the lower concentration of RBS demonstrated lower toxicity towards U87 and U–CH1 cells and maintained stable chemical properties under 808 nm NIR irradiation, without showing toxic effects against U87 and U–CH1 cells.

4.1.2. Analysis of migration and invasion ability of U87 and U–CH1 cells by 808 nm NIR-irradiated UCNPs@mSiO$_2$-NH$_2$&RBS

Migration and invasion are the two main characteristics of abnormal tumor cell proliferation. Cell scratch and cell transwell assays are commonly used methods to study the characteristics of tumor cell proliferation in plane and space. As shown in Fig. 12 (A), the scratch area assay showed the results of lateral cell migration. After 24 h of cell treatment, the changes in the scratch area of U87 and U–CH1 cells in the NIR group versus the UCNPs@mSiO$_2$-NH$_2$&RBS group were smaller compared to the Control group (p > 0.05). However, the 808 nm NIR-excited UCNPs@mSiO$_2$-NH$_2$&RBS group displayed 2.9 times and 1.6 times more scratch area than the Control group for U87 and U–CH1 cells, respectively (p < 0.001). The results of the cell invasion experiment are shown in Fig. 12 (B). After 24h of cell treatment, the number of tumor cells invaded in the NIR group had little change compared to the Control group (p > 0.05). The number of U87 and U–CH1 invasive cells in the UCNPs@mSiO$_2$-NH$_2$&RBS group was decreased by 0.5 and 0.9 times compared to that in the Control group (p < 0.01), showing some inhibition of cell invasion. In the 808 nm NIR-excited UCNPs@mSiO$_2$-
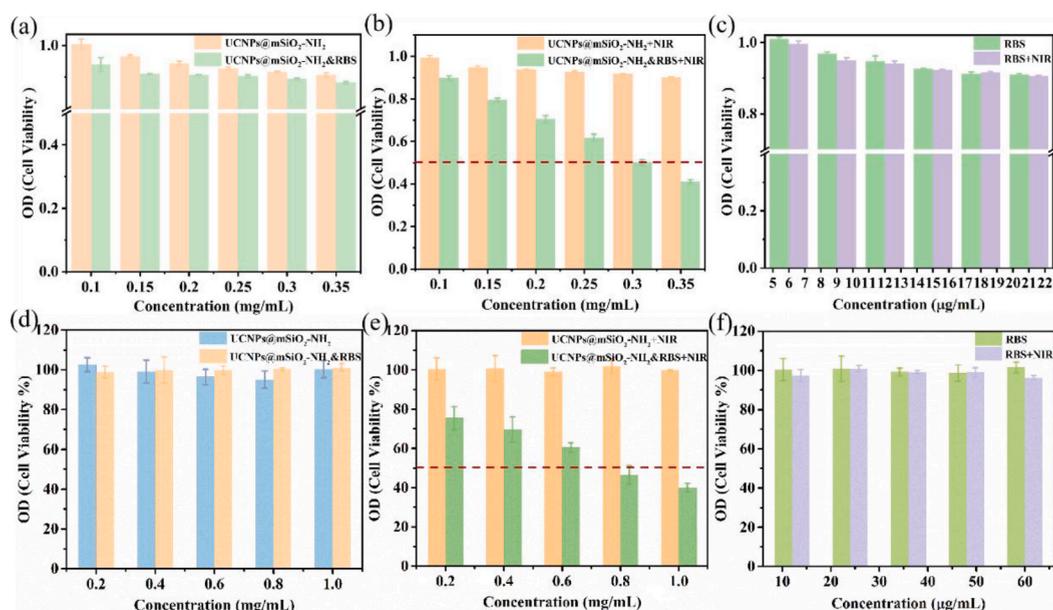

Fig. 11. The viability of U87 cells and U–CH1 cells was measured by CCK-8 assay. (a) Toxicity of different concentrations of UCNPs@mSiO$_2$-NH$_2$, UCNPs@mSiO$_2$-NH$_2$&RBS on glioma U87 cells, (b) Toxicity of 808 nm NIR lighted different concentrations of UCNPs@mSiO$_2$-NH$_2$, UCNPs@mSiO$_2$-NH$_2$&RBS on glioma U87 cells cells, (c) Toxicity of RBS, 808 nm NIR lighted RBS on glioma U87 cells, (d) Toxicity of different concentrations of UCNPs@mSiO$_2$-NH$_2$, UCNPs@mSiO$_2$-NH$_2$&RBS on chordoma U–CH1 cells, (e) Toxicity of 808 nm NIR lighted different concentrations of UCNPs@mSiO$_2$-NH$_2$, UCNPs@mSiO$_2$-NH$_2$&RBS on chordoma U–CH1 cells, (f) Toxicity of RBS, 808 nm NIR lighted RBS on chordoma U–CH1 cells.
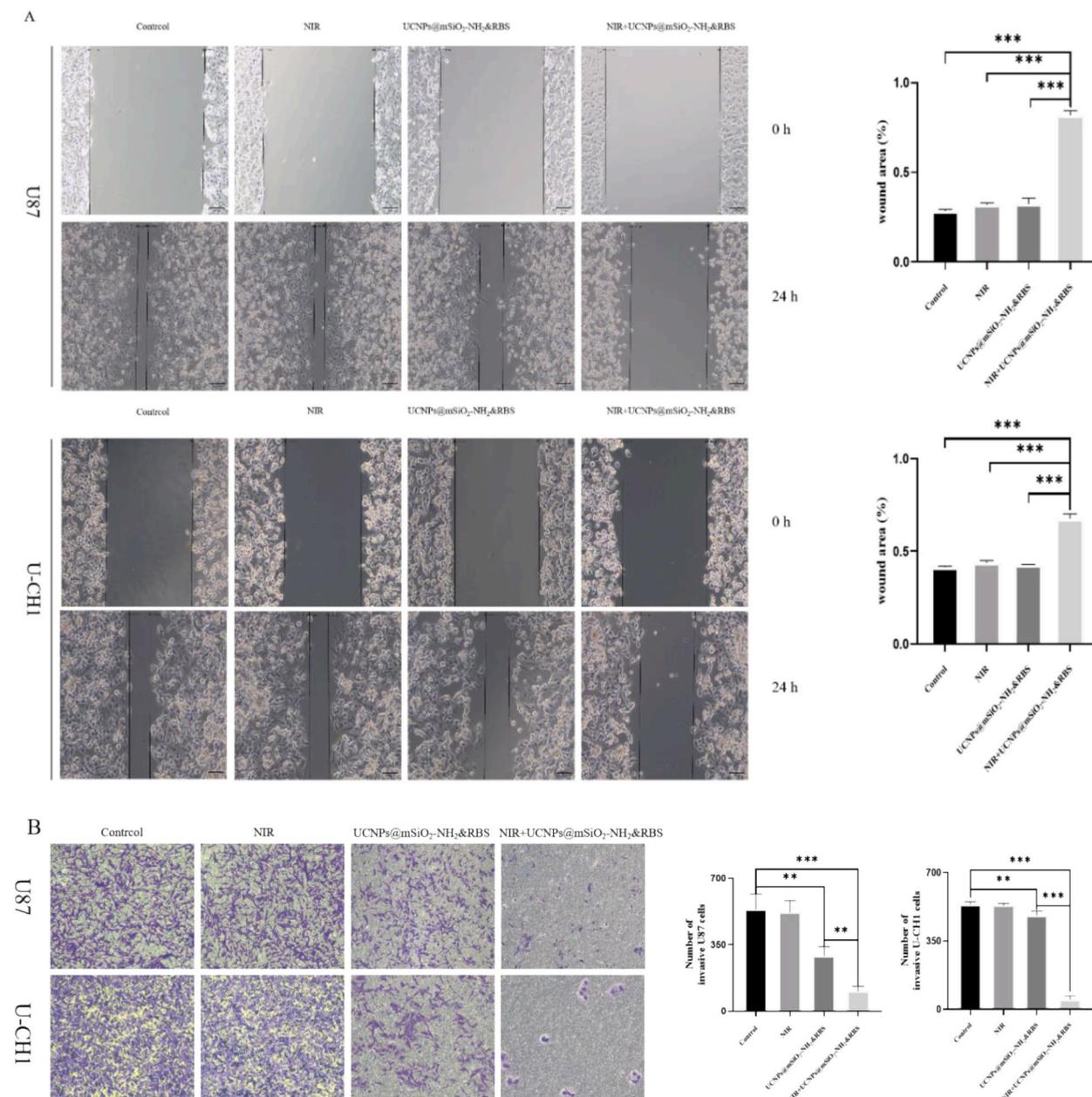
Fig. 12. Invasion and migration assay in vitro. (A) The migration ability of U87 cells, U–CH1 cells using scratch area under different treatment conditions. (B) The invasion ability of U87 cells and U–CH1 cells in Transwell chambers (8 μm/well) under different treatment conditions. Data are presented as the mean ± standard deviation. (n = 3), **p < 0.01, ***p < 0.001.

NH$_2$&RBS group, the number of U87 and U–CH1 invasive cells was reduced to 0.2 times and 0.1 times, respectively, compared to the Control group (p < 0.001), demonstrating a significant inhibition of cell invasion. The experimental results validate that NO released from UCNPs@mSiO$_2$-NH$_2$&RBS shows an inhibitory effect on the migration and invasive ability of brain tumor cells after exposure to NIR light.

4.2. Analysis of tumor cell apoptosis promotion ability of UCNPs@mSiO$_2$-NH$_2$&RBS by 808 nm NIR excitation

4.2.1. Analysis of Calcein-AM/PI double staining method to characterize the ability of NO to kill tumor cells

Fa et al. [29] developed a core-shell structure using NaYF$_4$: Tm/Yb/Ca@NaGdF$_4$: Nd/Yb UCNPs loaded with the photosensitizing NO donor S-nitroso-N-acetyl-DL-penicillamine. The developed system achieved photocontrolled release of NO upon stimulation with NIR, while the concentration of NO exhibited a toxic effect on HepG2. To this end, we characterized whether NO release from 808 nm

NIR irradiated UCNPs@mSiO$_2$-NH$_2$&RBS promoted brain tumor cell death by Calcein-AM/PI double staining. As shown in Fig. 13 (A), Calcein-AM specifically labeled live cells and PI specifically labeled dead cells. No obvious tumor cell death was observed in the Control, NIR, and UCNPs@mSiO$_2$-NH$_2$&RBS groups. However, the 808 nm NIR-irradiated UCNPs@mSiO$_2$-NH$_2$&RBS group showed a significant ability to induce tumor cell death. This suggests that UCNPs@mSiO$_2$-NH$_2$&RBS, when irradiated by 808 nm NIR light, release a large amount of NO, leading to the death of U87 cells. Similarly, as shown in Fig. 13 (B), it is evident that 808 nm NIR light irradiation of UCNPs@mSiO$_2$-NH$_2$&RBS can effectively release NO, thus promoting chordoma cell death.

4.2.2. Analysis of NO's ability to promote apoptosis in tumor cells

Li's group [14] designed and developed a NIR-excited NO delivery nanoplatform for overcoming multidrug resistance (MDR) in tumor cells. They employed UCNP@MgSiO$_3$ loaded with PH-sensitive doxorubicin (DOX), thereby achieving simultaneous NO triggering and DOX release. This combined treatment strategy induced apoptosis of MDR cells and inhibited the growth of MDR tumors *in vivo*. To this end, we further quantified the number of apoptotic tumor cells by flow cytometry (Annexin V/PI double staining), as shown in Fig. 14(A) and (B), the total number of apoptotic tumor cells in the NIR group and the UCNPs@mSiO$_2$-NH$_2$&RBS-treated group was not significantly affected compared to the Control group ($p > 0.05$). However, the 808 nm NIR light irradiation of the UCNPs@mSiO$_2$-NH$_2$&RBS-treated U87 and U–CH1 cells showed 5.0 and 3.2 times more apoptosis than that of the Control group, respectively ($p < 0.001$). This suggests that 808 nm NIR irradiation of UCNPs@mSiO$_2$- NH$_2$&RBS's optical platform can effectively release NO, inducing apoptosis and necrosis of brain tumor cells.

4.2.3. Mechanistic analysis of NO-induced apoptosis in tumor cells characterized by Western-blotting

Mitochondria, as the main energy source of cells, are also the target organ of NO-regulated cells [30]. NO and pro-apoptotic
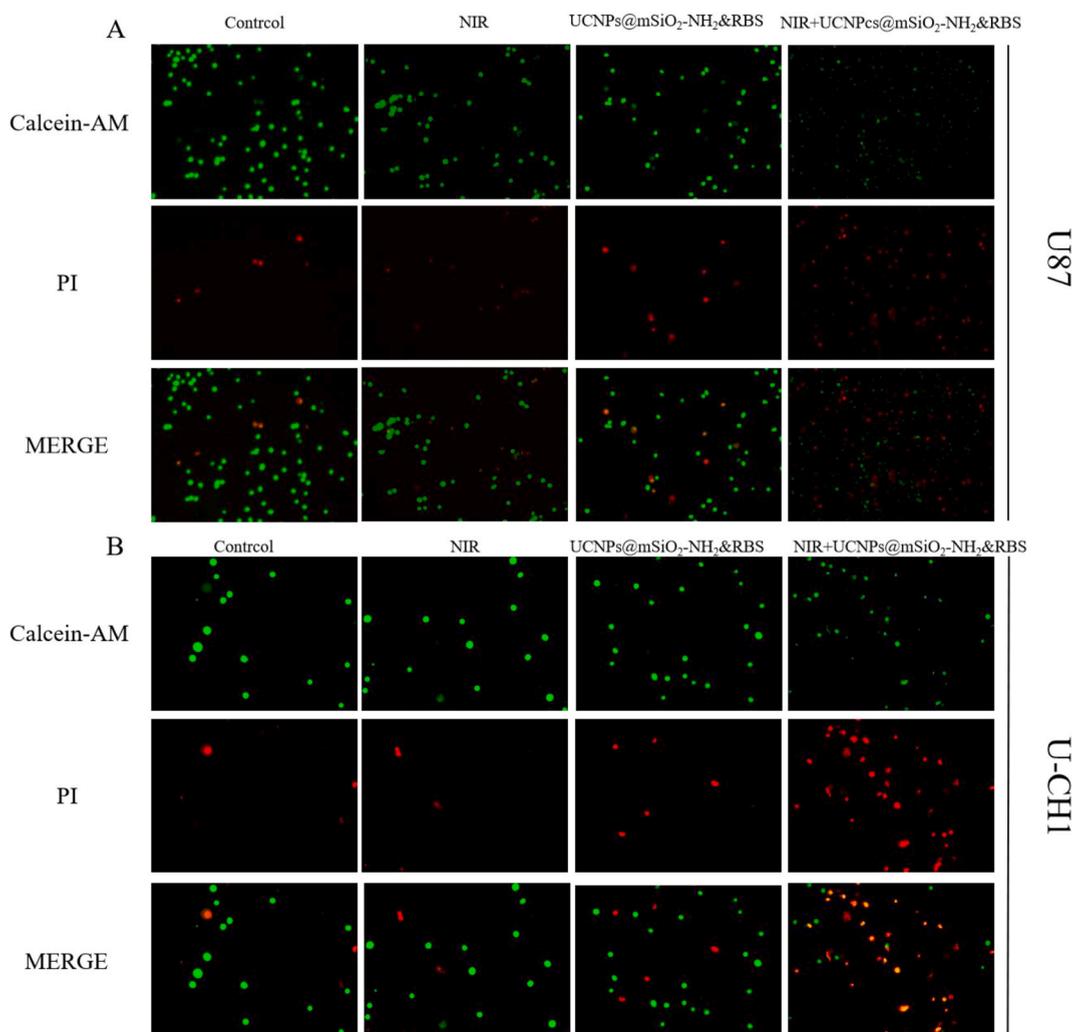

Fig. 13. Calcein-AM/PI double staining was used to detect the survival and death of cells. (A) Fluorescence images of live and dead cells stained by different treatments on U87 cells. (B) Fluorescence images of live and dead cell staining by different treatments on U–CH1 cells.
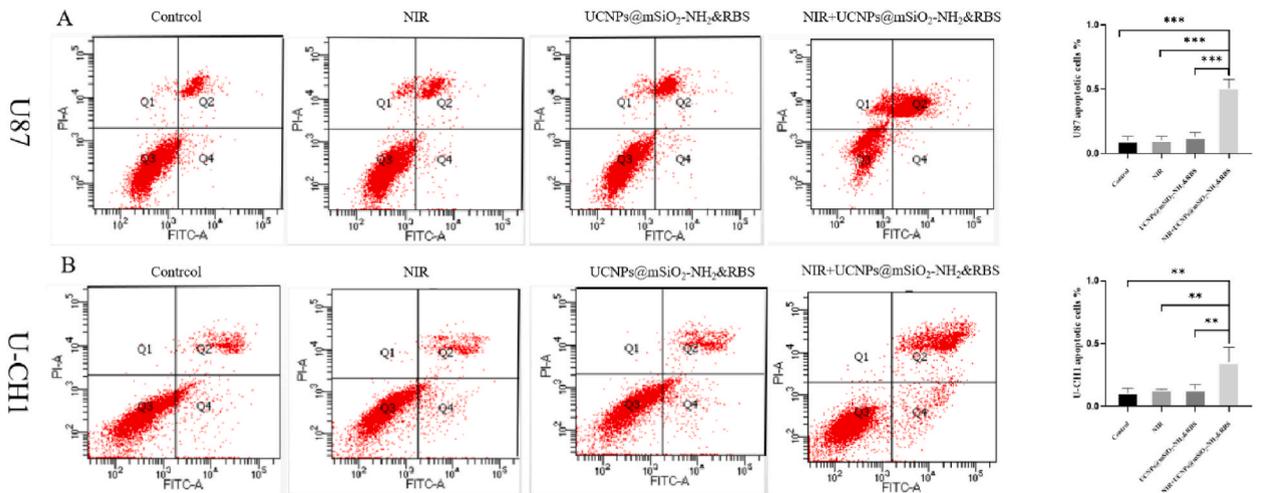
Fig. 14. The number of apoptotic cells was detected by flow cytometry. (A) Apoptosis of U87 cells under different conditions. (B) Apoptosis of U–CH1 cells under different conditions. Data are presented as the mean ± standard deviation. (n = 3), **$p < 0.01$, ***$p < 0.001$.

proteins induce the release of apoptotic factors and mitochondrial caspases into the cytoplasm by increasing the permeability of the mitochondrial membrane, leading to apoptosis [31,32]. Caspase-3 is one of the most critical enzymes in the apoptosis pathway. Relevant apoptotic proteins were detected by Western blotting to investigate the molecular mechanism of apoptosis occurring in U87 cells. As shown in Fig. 15, there was no significant difference in the expression of apoptosis-related proteins in tumor cells treated with NIR and UCNPs@mSiO$_2$-NH$_2$&RBS groups compared with the Control group (p > 0.05). However, the 808 nm NIR-excited UCNPs@mSiO$_2$-NH$_2$&RBS group treated tumor cells showed 3.0 times higher expression of Caspase-3 than the Control group (p < 0.001). In conclusion, 808 nm NIR irradiation of UCNPs@mSiO$_2$-NH$_2$&RBS can effectively release NO and promote tumor cell apoptosis by changing the expression of apoptosis-related protein markers Caspase-3.

4.3. Therapeutic analysis of NO on tumors in vivo

The therapeutic efficacy of NO release from UCNPs@mSiO$_2$-NH$_2$&RBS under 808 nm NIR light was investigated *in vivo* through brain tumor transplantation in a mouse model and the molecular outcomes were then evaluated. As shown in Fig. 16(A), we first constructed a xenograft tumor mouse model, and then administered UCNPs@mSiO$_2$-NH$_2$&RBS drug injection to the tumor localization, and irradiated the tumor site with 808 nm NIR after 24 h. The UCNPs@mSiO$_2$-NH$_2$&RBS in the tumor tissues as well as uptaken by the cells under the laser light produced a relatively high concentration of NO, the Nitrosyl and oxidative reactions with intracellular reactive oxygen species lead to impaired cell function, which in turn promotes tumor cell necrosis or apoptosis. The tumors of mice after treatment were compared, as shown in Fig. 16(B), the tumor volumes of glioma and chordoma in the Control group were 1.1 times and 1 times of those in the UCNPs@mSiO$_2$-NH$_2$&RBS group, respectively. Is 5.5 times and 3.7 times of 808 nm NIR excited UCNPs@mSiO$_2$-NH$_2$&RBS group. All the tumor-bearing mice survived at the end of the treatment as shown in Fig. 16(C). Similarly, there was no significant change in the body weight of the mice during the treatment period, indicating the low cytotoxicity of
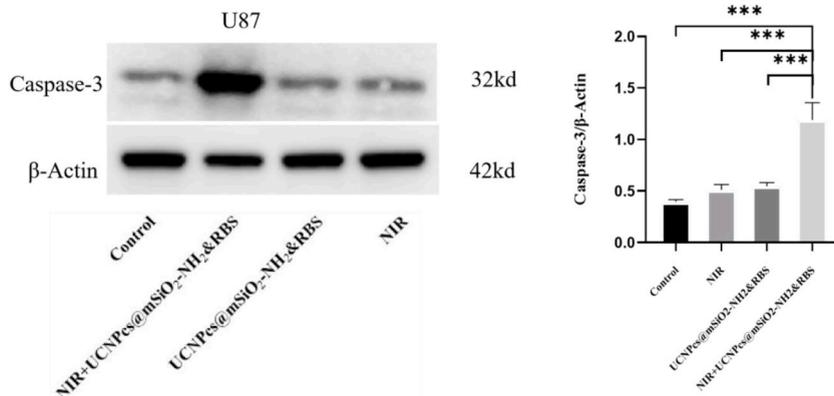

Fig. 15. Expression of apoptosis-related proteins Caspase-3 in U87 cells.Data are presented as the mean ± standard deviation. (n = 3), ***p < 0.001.
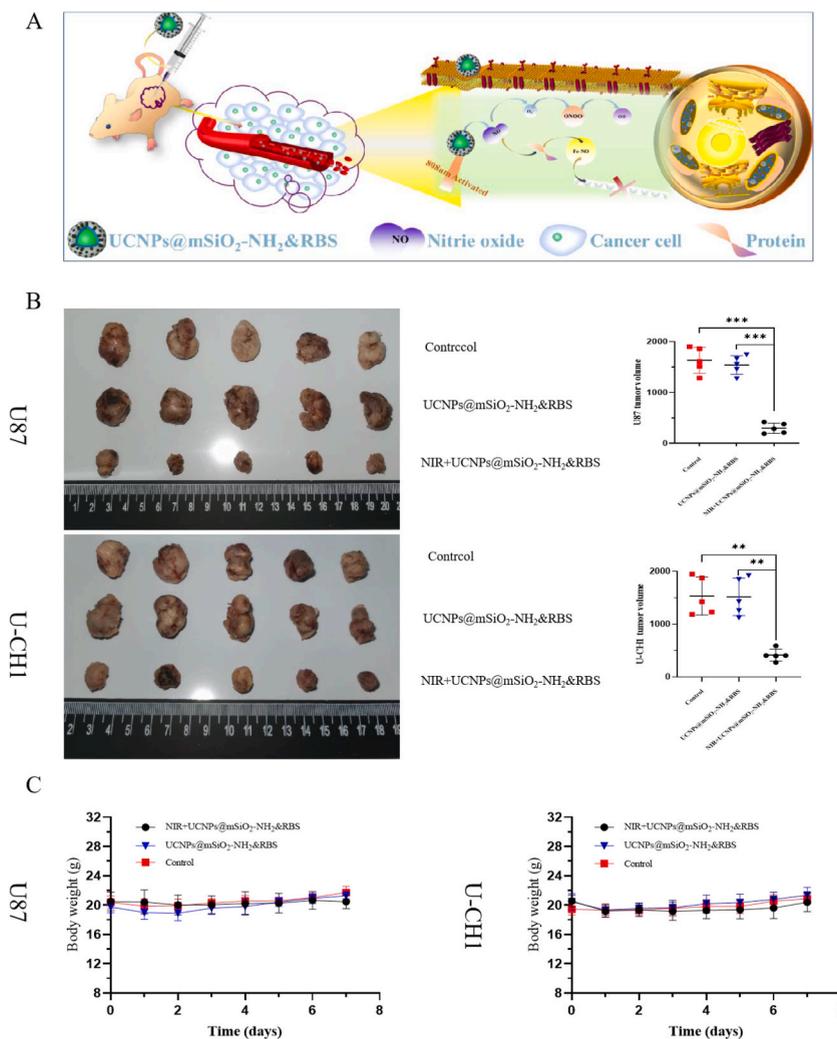
Fig. 16. Changes in tumor volume and mouse body weight in xenograft tumor-bearing mice treated with NO. (A) Schematic representation of NO treatment of xenograft tumor-bearing mice. (B) Comparison of xenograft tumor volume among three groups. (C) The body weight of tumor-bearing mice shows no notable change during the experimental period. Data are presented as the mean $\pm$ standard deviation. (n = 3), **p < 0.01, ***p < 0.001.

UCNPs@mSiO$_2$-NH$_2$&RBS on normal tissues. In this experiment, we investigated the therapeutic effect of NO released from UCNPs@mSiO$_2$-NH$_2$&RBS under 808 nm NIR excitation on brain tumor transplantation tumors, but the experimental period was relatively short, and the long-term therapeutic effect was not followed up; moreover, we constructed a model of xenotransplantation tumors in nude mice in the present study, which is still slightly insufficient in comparison with the therapeutic efficacy and reliability of the transplantation tumors in situ.

Tumor tissues obtained from the Control, UCNPs@mSiO$_2$-NH$_2$&RBS, and 808 nm NIR-excited UCNPs@mSiO$_2$-NH$_2$&RBS groups were sectioned. The pathological changes in tumor tissues were observed by Hematoxylin and Eosin (H&E) staining and the results are shown in Fig. 17(A). The tumor tissues in the Control and UCNPs@mSiO$_2$-NH$_2$&RBS groups showed an increase in pathological mitoses and trophoblast vessels. However, the 808 nm NIR-excited UCNPs@mSiO$_2$-NH$_2$&RBS group had condensed cellular chromatin, the nuclei were plasmid-dense or cleaved, and the number of trophoblast vessels was significantly reduced.

The expression of ki-67 was further detected to understand the proliferative capacity of tumor cells and the results are shown in Fig. 17(B). Ki-67 expression in glioma and chordoma tissues of the Control group was 1.0 and 1.1 times that of the UCNPs@mSiO$_2$-NH$_2$&RBS group, respectively (p > 0.05). In contrast, it was 4.0 times (p < 0.001) and 10 times (p < 0.01) higher than that of the 808 nm NIR-excited UCNPs@mSiO$_2$-NH$_2$&RBS group. These results confirm that the release of NO from UCNPs@mSiO$_2$-NH$_2$&RBS under NIR light significantly attenuated the pathological deterioration in glioma and chordoma models.
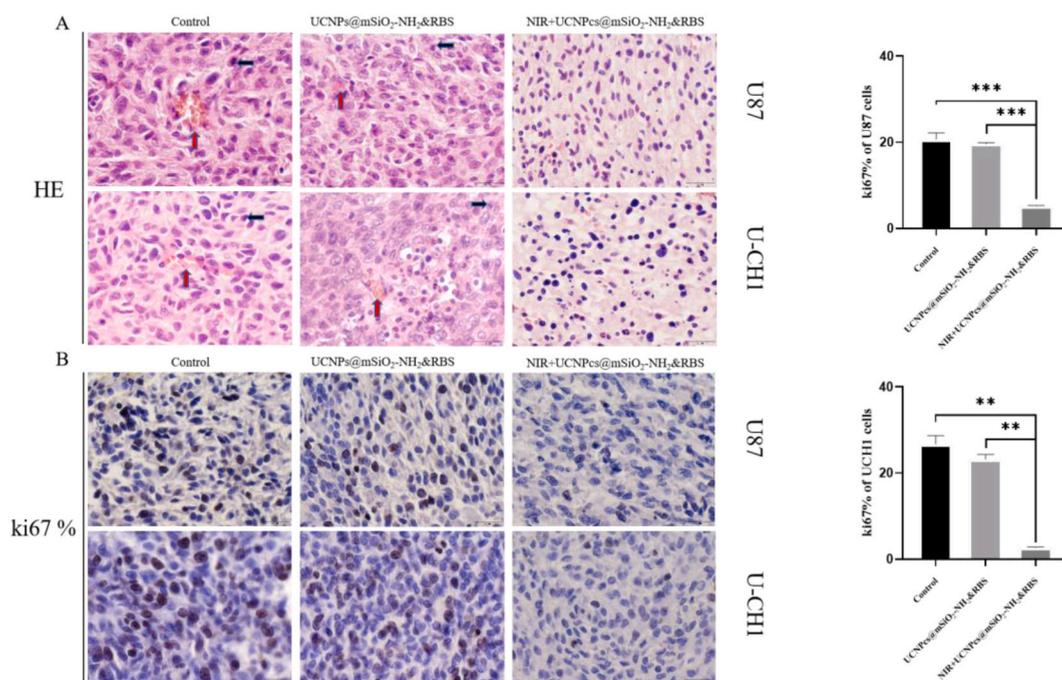
Fig. 17. Pathological changes in the tumor samples. (A) The histological changes were observed by H&E staining. The pathological mitosis is indicated by a black arrow, while the nourishing vessels are represented by a red arrow. (B) Ki67 expression is detected by IHC. Data are presented as the mean $\pm$ standard deviation. (n = 3), **$p < 0.01$,***$p < 0.001$.

5. Conclusions

In conclusion, this study constructed a photocontrolled NO release platform through NIR photoexcitation of UCNPs@mSiO$_2$-NH$_2$&RBS. The concentration-dependent increase in NO release, as evident from the results of the CCK-8 assay, showed a significant reduction in the activity of glioma and chordoma cells, along with inhibition of their migratory and invasive abilities. Further, the constructed platform effectively decreased the growth rate of tumors in mice model. This efficient treatment strategy not only addresses the challenge of limited laser penetration depth in traditional photodynamic therapies for tumors but also presents efficiency for brain tumor therapy. Despite these potential applications, limitations include the need for multiple injections within a short period during *in vivo* experiments and the lack of selective tumor targeting. Further studies should focus on improving the targeting capabilities of the photocontrolled release platform and addressing biosafety concerns associated with the long-term persistence of UCNPs in living organisms.

High concentration of NO gas has excellent anti-tumor ability and has a broad application in tumor therapy. In this study, we constructed a photocontrolled NO release platform of UCNPs@mSiO$_2$-NH$_2$&RBS under 808 nm excitation to promote the apoptosis of glioma and chordoma cells through the effective release of NO, and to reduce the growth rate of tumors in nude mice. However, the NO release platform lacks tumor targeting, so there is still much room for the development of targeted tumor modification of this photocontrolled release platform; Meanwhile, in view of the complexity of the nanomedicine carrier system, the long-term existence of this type of structure in the organism is still a biosafety issue. Therefore, more studies on the long-term stability of nanomedicines in organisms are needed.

Data availability statement

The data that support the findings of this study are available on request from the corresponding author (Xue-wei Xia: 824759672@qq.com).

CRediT authorship contribution statement

Lei Li: Writing – original draft, Validation, Software, Project administration, Methodology, Investigation, Data curation, Conceptualization. **Jiang-hua Yang:** Writing – original draft, Validation, Software, Methodology, Investigation, Data curation, Conceptualization. **Xin-meng Fa:** Software, Methodology, Conceptualization. **Ming-song Liu:** Software, Methodology, Data curation. **Qi-lin Wang:** Software, Methodology. **Tong-fei Zeng:** Software, Project administration, Methodology. **Rui-zhe Chen:** Software, Data curation. **Jun Ou:** Writing – review & editing, Visualization, Software, Methodology, Data curation, Conceptualization. **Xue-wei Xia:** Writing – review & editing, Software, Resources, Methodology, Funding acquisition, Data curation, Conceptualization.

Declaration of competing interest

The authors declare that they have no known competing financial interests or personal relationships that could have appeared to influence the work reported in this paper.

Acknowledgments

Appendix A. Supplementary data

Supplementary data to this article can be found online at https://doi.org/10.1016/j.heliyon.2024.e33576.

References

[1] B. Lucke-Wold, B.S. Rangwala, M.A. Shafique, et al., Focus on current and emerging treatment options for glioma: a comprehensive review, World J. Clin. Oncol. 15 (4) (2024) 482–495, https://doi.org/10.5306/wjco.v15.i4.482.
[2] Z. Yang, C. Zhao, S. Zong, J. Piao, Y. Zhao, X. Chen, A review on surgical treatment options in gliomas, Front. Oncol. 13 (2023) 1088484, https://doi.org/10.3389/fonc.2023.1088484. Published 2023 Mar 16.
[3] L.B. Palavani, L. de Barros Oliveira, P.A. Reis, et al., Efficacy and safety of intraoperative radiotherapy for high-grade gliomas: a systematic review and meta-analysis, Neurosurg. Rev. 47 (1) (2024) 47, https://doi.org/10.1007/s10143-024-02279-2. Published 2024 Jan 15.
[4] P. Verma, H. Joshi, T. Singh, et al., Temozolomide and flavonoids against glioma: from absorption and metabolism to exosomal delivery, Naunyn-Schmiedeberg's Arch. Pharmacol. 397 (1) (2024) 41–57, https://doi.org/10.1007/s00210-023-02660-w.
[5] E. Agosti, M. Zeppieri, L. De Maria, et al., Glioblastoma immunotherapy: a systematic review of the present strategies and prospects for advancements, Int. J. Mol. Sci. 24 (20) (2023) 15037, https://doi.org/10.3390/ijms242015037. Published 2023 Oct 10.
[6] L. Denaro, A. Berton, M. Ciuffreda, et al., Surgical management of chordoma: a systematic review, J Spinal Cord Med. 43 (6) (2020) 797–812, https://doi.org/10.1080/10790268.2018.1483593.
[7] W. Domka, D. Bartusik-Aebisher, I. Rudy, K. Dynarowicz, K. Pięta, D. Aebisher, Photodynamic therapy in brain cancer: mechanisms, clinical and preclinical studies and therapeutic challenges, Front. Chem. 11 (2023) 1250621, https://doi.org/10.3389/fchem.2023.1250621. Published 2023 Nov 24.
[8] T. Hsia, J.L. Small, A. Yekula, et al., Systematic review of photodynamic therapy in gliomas, Cancers 15 (15) (2023) 3918, https://doi.org/10.3390/cancers15153918. Published 2023 Aug 1.
[9] D. Aebisher, A. Przygórzewska, A. Myśliwiec, et al., Current photodynamic therapy for glioma treatment: an update, Biomedicines 12 (2) (2024) 375, https://doi.org/10.3390/biomedicines12020375. Published 2024 Feb 6.
[10] W. Stummer, M. Müther, D. Spille, Beyond fluorescence-guided resection: 5-ALA-based glioblastoma therapies, Acta Neurochir. 166 (1) (2024) 163, https://doi.org/10.1007/s00701-024-06049-3. Published 2024 Apr 2.
[11] Y. Cheng, H. Cheng, C. Jiang, et al., Perfluorocarbon nanoparticles enhance reactive oxygen levels and tumour growth inhibition in photodynamic therapy, Nat. Commun. 6 (2015) 8785, https://doi.org/10.1038/ncomms9785. Published 2015 Nov 3.
[12] M.M. Kim, A. Darafsheh, Light sources and dosimetry techniques for photodynamic therapy, Photochem. Photobiol. 96 (2) (2020) 280–294, https://doi.org/10.1111/php.13219.
[13] N. Yang, F. Gong, L. Cheng, Recent advances in upconversion nanoparticle-based nanocomposites for gas therapy, Chem. Sci. 13 (7) (2021) 1883–1898. Published 2021 Dec 14.
[14] S. Li, X. Song, X. Zhu, et al., Light-switchable yolk-mesoporous shell UCNPs@MgSiO3 for nitric oxide-evoked multidrug resistance reversal in cancer therapy, ACS Appl. Mater. Interfaces 12 (27) (2020) 30066–30076.
[15] B. Zhou, X. Sun, B. Dong, et al., Antibacterial PDT nanoplatform capable of releasing therapeutic gas for synergistic and enhanced treatment against deep infections, Theranostics 12 (6) (2022) 2580–2597. Published 2022 Feb 28.
[16] M. Maniscalco, S. Fuschillo, I. Mormile, et al., Exhaled nitric oxide as biomarker of type 2 diseases, Cells 12 (21) (2023) 2518, https://doi.org/10.3390/cells12212518. Published 2023 Oct 25.
[17] Y. Jiang, P. Fu, Y. Liu, C. Wang, P. Zhao, X. Chu, X. Jiang, W. Yang, Y. Wu, Y. Wang, G. Xu, J. Hu, W. Bu, Near-infrared light-triggered NO release for spinal cord injury repair, Sci. Adv. 6 (39) (2020 Sep 25) eabc3513, https://doi.org/10.1126/sciadv.abc3513. PMID: 32978153; PMCID: PMC7518874.
[18] H. Ding, J. Chang, F. He, S. Gai, P. Yang, Hydrogen sulfide: an emerging precision strategy for gas therapy, Adv Healthc Mater 11 (4) (2022) e2101984.
[19] R. Gu, L. Wang, X. Huang, et al., pH/glutathione-responsive release of SO_2 induced superoxide radical accumulation for gas therapy of cancer, Chem. Commun. 56 (94) (2020) 14865–14868.
[20] L. Feng, R. Zhao, B. Liu, et al., Near-infrared upconversion mesoporous tin oxide bio-photocatalyst for H2O2-activatable O2-generating magnetic targeting synergetic treatment, ACS Appl. Mater. Interfaces 12 (37) (2020) 41047–41061.
[21] C. Wu, P. Zou, S. Feng, et al., Molecular hydrogen: an emerging therapeutic medical gas for brain disorders, Mol. Neurobiol. 60 (4) (2023) 1749–1765, https://doi.org/10.1007/s12035-022-03175-w.
[22] Y. Opoku-Damoah, R. Zhang, H.T. Ta, Z.P. Xu, Vitamin E-facilitated carbon monoxide pro-drug nanomedicine for efficient light-responsive combination cancer therapy, Biomater. Sci. 9 (18) (2021) 6086–6097. Published 2021 Sep. 14.
[23] J.O. Lundberg, E. Weitzberg, Nitric oxide signaling in health and disease, Cell 185 (16) (2022) 2853–2878, https://doi.org/10.1016/j.cell.2022.06.010.
[24] S.X. Liu, G.W. Li, D. Ma, Controllable nitric oxide-delivering platforms for biomedicalapplications, Advanced Therapeutics 5 (3) (2022) 2100227.
[25] H. Yu, A. Tiemuer, X. Yao, et al., Mitochondria-specific near-infrared photoactivation of peroxynitrite upconversion luminescent nanogenerator for precision cancer gas therapy, Acta Pharm. Sin. B 14 (1) (2024) 378–391, https://doi.org/10.1016/j.apsb.2023.08.019.
[26] J.P. Wittke, I. Ladany, P.N. Yocom, Y2O3:Yb:Er-new red-emitting infrared-excited phosphor, J. Appl. Phys. 43 (2) (1972) 595–600.
[27] J. Taylor, C. Litwinski, T. Nyokong, E. Antunes, Fluorescence behaviour of an aluminium octacarboxy phthalocyanine–NaYGdF4:Yb/Er nanoparticle conjugate, J. Fluoresc. 25 (3) (2015) 489–501.
[28] J. Zhao, Y. Hu, S.W. Lin, et al., Enhanced luminescence intensity of near-infrared-sensitized upconversion nanoparticles via Ca2+ doping for a nitric oxide release platform, J. Mater. Chem. B 8 (30) (2020) 6481–6489.
[29] X. Fa, S. Lin, J. Yang, et al., 808 nm-activated Ca2+doped up-conversion nanoparticles that release no inducing liver cancer cell (HepG2) apoptosis, Methods Appl. Fluoresc. 10 (2) (2022), https://doi.org/10.1088/2050-6120/ac5524. Published 2022 Feb 23.

[30] A. Sahebnasagh, F. Saghafi, S. Negintaji, et al., Nitric oxide and immune responses in cancer: searching for new therapeutic strategies, Curr. Med. Chem. 29 (9) (2022) 1561–1595.

[31] F.H. Khan, E. Dervan, D.D. Bhattacharyya, J.D. McAuliffe, K.M. Miranda, S.A. Glynn, The role of nitric oxide in cancer: master regulator or NOt? Int. J. Mol. Sci. 21 (24) (2020) 9393. Published 2020 Dec 10.

[32] Z. Zhou, Z. Gao, W. Chen, et al., Nitric oxide-mediated regulation of mitochondrial protective autophagy for enhanced chemodynamic therapy based on mesoporous Mo-doped Cu9S5 nanozymes, Acta Biomater. 151 (2022) 600–612, https://doi.org/10.1016/j.actbio.2022.08.011.